A New Approach for the Enhancement of Dual-energy Computed Tomography Images

by

Kyung Kook Park

A Dissertation Presented in Partial Fulfillment
of the Requirements for the Degree
Doctor of Philosophy

Approved January 2011 by the
Graduate Supervisory Committee:

Metin Akay, Chair
William Pavlicek
Yasemin Akay
Bruce Towe
Jitendran Muthuswamy

ARIZONA STATE UNIVERSITY

May 2011

ABSTRACT

Computed tomography (CT) is one of the essential imaging modalities for medical diagnosis. Since its introduction in 1972, CT technology has been improved dramatically, especially in terms of its acquisition speed. However, the main principle of CT which consists in acquiring only density information has not changed at all until recently. Different materials may have the same CT number, which may lead to uncertainty or misdiagnosis. Dual-energy CT (DECT) was reintroduced recently to solve this problem by using the additional spectral information of X-ray attenuation and aims for accurate density measurement and material differentiation. However, the spectral information lies in the difference between two low and high energy images or measurements, so that it is difficult to acquire the accurate spectral information due to amplification of high pixel noise in the resulting difference image. In this work, a new model and an image enhancement technique for DECT are proposed, based on the fact that the attenuation of a high density material decreases more rapidly as X-ray energy increases. This fact has been previously ignored in most of DECT image enhancement techniques. The proposed technique consists of offset correction, spectral error correction, and adaptive noise suppression. It reduced noise, improved contrast effectively and showed better material differentiation in real patient images as well as phantom studies.

ACKNOWLEGEMENTS

Finally, I stand as a researcher on my own feet. I thank my friends, David Akkur, Andrei Dracomir, Dominique Gauthier, Jeremy F. Romain and Didem Yamak. They made my wonderful life here in Arizona State University. I thank Thomas Boltz, Robert Paden, Mary Beth, Physics team members of Mayo Clinic, Scottsdale. It was my great opportunity to work with them and learned a lot from their enthusiasm and professional performance. And, I would like to express special thanks to Dr. William Pavlicek. He gave me the opportunity to work CT imaging and guided me to advance in this field. I thank Dr Yasemin Akay for her guidance and kindness. I am deeply grateful to my advisor, Professor Metin Akay. Without his endless support, guidance and inspiration, I could not have finished this work.

And, I thank my mother and father.

TABLE OF CONTENTS

Page

CHAPTER

LIST OF TABLES

Table Page

LIST OF FIGURES

CHAPTER 1

INTRODUCTION

Computed tomography (CT) is one of the essential imaging modalities for medical diagnosis. Since its introduction by Godfrey Hounsfield in 1972 [1], CT technology has been innovated dramatically, especially in its acquisition speed. A current commercial CT machine has achieved 75ms temporal resolution and can acquire the entire heart which beats even at 120 bpm with minimum cardiac motion artifacts [2]. However, the main principle of CT consists of acquiring only density information, which has not changed at all until recently. It is the problem of the conventional CT imaging that different materials of similar density can have the similar CT number, and it may lead to misdiagnosis or uncertainty. Dual-energy CT (DECT) was reintroduced recently to solve the problem by using the additional information of energy dependency of X-ray attenuation of body tissues.

DECT has a history as long as CT. Soon after CT became available for clinical purposes, beam hardening or spectral artifact was observed in a material of high X-ray attenuation and caused nonlinear and unexpected distortion in the resulting images [3]. At first, several research groups began to use the dual-spectral information of X-ray to correct the spectral artifacts [4-7] and also suggested a possibility to use DECT for direct tissue characterization of fatty liver, kidney stone and bone densitometry [8-17]. In the late 80’s, the first commercial DECT (SOMATO DR) using fast-voltage-switching was introduced by Siemens, (Forchheim, Germany), but it was not further developed. No clinical advantage was proved except for bone densitometry. It was mainly due to the practical limitation at that time such as poor CT machine performance, cost and radiation dose, while several research groups did research on DECT to develop techniques or presented theoretical background for the clinical application of DECT using simulation and phantom studies. In the 80's, most current theory of DECT such as material decomposition was already established. The theoretical background of DECT is reviewed in the next chapter.

In 2006, Siemens introduced a revolutionary dual-source CT (DSCT). It has two X-ray source-detector pairs operating orthogonally and simultaneously at 90-degree offset in one gantry. It can operate at the single-energy or dual-energy modes by setting two X-ray sources operating at the same or different energy levels. Its temporal resolution was remarkable 83ms at the single-energy mode and 165ms at the dual-energy mode. Its high temporal resolution of the single-energy mode has made possible cardiac imaging even up-to 120-bpm heart beats with minimum cardiac motion artifacts [18]. Soon after the introduction of DSCT, most researches have been paying attention to its cardiac imaging application using the fast single-energy mode [18-28]. Relatively few clinical evaluations of dual-energy cardiac imaging using its dual-scan mode were reported. It did not take long time for clinical evaluations of dual-energy mode of DSCT to be reported and to show feasible clinical applications of DECT:

Kidney stone characterization [29-31],
Fat or iron composition in the liver [32] [33],
Discrimination of cyst and malignant tumors of liver [34]
Lung cancer detection [35]
Lung perfusion imaging and pulmonary embolism [36-39]
Coronary artery stenosis [40]
Image segmentation like bone or plaque removal and ligaments or tendons identification [41]
Myocardial ischemia perfusion imaging [42]

Application for postmortem CT [43]

Urinary Stone characterization [44, 45].

Currently, the most widely-used DECT technique for clinical application is three-material decomposition presented by Johnson et al. [30]. In their initial evaluation of DSCT, they introduced a new tissue characterization method using the dual-energy mode of DSCT. The three-material decomposition is based on the tissue signature plot, in which one-pair of CT values of low (80kVp) and high energy (140kVp) images defines tissue attenuation. The relative position of tissue in the tissue signature plot represents how much the tissues are close to fat, soft tissue and iodine, and it is processed for material differentiation. After the three-material decomposition, the color-coded tissue types are overlaid for easy recognition of each tissue properties on the virtual 120kVp image, the weighted sum of low and high energy images (30% of 80kVp and 70% of 140kVp). Using DSCT, Johnson et al. also demonstrated several promising applications of DECT such as virtual non-enhanced (VNE) CT imaging by removing the iodine content of the contrast-enhanced CT images and automatic bone removal. However, they did not presented clearly how the three-material decomposition was implemented it and how they solved the noise problem of DECT.

Since the introduction of DSCT, radiologists confirmed the usefulness of virtual 120kVp image and virtual non-contrast images of DECT. The virtual 120kVp image of DECT has similar quantification ability to the standard 120kVp CT imaging [18, 46] and so helps radiologist to compare the new DECT results with the criteria of standard 120kVp CT imaging which has been established over 30 years of CT imaging. Radiologists also confirmed that the virtual non-enhanced images can replace pre-contrast CT imaging and so it reduces the total radiation dose by skipping the pre-contrast CT imaging which is included in typical contrast-enhanced CT protocols [47], even though DECT intrinsically requires the additional dose.

The work of Ruzsics et al. [42] is a good example of application of the three material decomposition and shows the potential of DECT. In their initial work, they found that myocardial ischemia diagnosed by iodine maps of DECT is highly correlated with single-photon emission computed tomography (SPECT). In addition, they also evaluated coronary stenosis and myocardial ischemia of thirty-five patient study using DECT and reported that the results were well-correlated with SPECT, coronary catheterization and coronary CT angiography. More specifically, coronary CT angiography had 98% sensitivity, 88% specificity and 92% accuracy for detection of >50% stenosis while DECT detected myocardial ischemia with 84% sensitivity, 94% specificity and 92% accuracy. It is important to notice that a single cardiac imaging with iodine contrast agent was performed for the comprehensive diagnosis of coronary stenosis and myocardial ischemia. For coronary stenosis detection, they used the virtual 120kVp images and investigated the coronary artery morphology as normal coronary angiography does. Myocardial ischemia was investigated using the color-coded iodine maps which were obtained by the three-material decomposition. They concluded that DECT can be an alternative of SPECT in near future.

Responding to Siemens' advance in CT, GE introduced Discovery CT750 HD (GE Healthcare, Milwaukee, WI, USA). It has a feature of fast voltage-switching dual energy mode [34, 48, 49] and acquires dual-energy scans with a single X-ray tube by alternating low and high kVps within several 0.3-0.5 milliseconds [2, 48]. In addition, GE approached DECT by using projection data. The raw projection data of low and high energy CT scans are decomposed into two-basis density maps before the image reconstruction and pseudo-monochromatic images are reconstructed by linear combination of the mass attenuation coefficients of the two basis materials weighted by their equivalent density maps on the workstation in real-time by user's control of energy level. Tkaczky et al. showed the feasibility of using the resulting density maps of material decomposition for discrimination of malignant tumor and cyst in liver and also suggested linear discrimination analysis to find optimal distinguishable energy level of the monochromatic images [34].

Recently, Karçaaltıncaba and Aktaş compared DSCT of Siemens Definitions including their new generation DSCT system (Definition flash) and GE Discovery 750HD for clinical applications in their review paper [2]. They even concluded that DECT can be an alternative to PET-CT. At this time, the clinical application of DECT is a very active topic in radiology. Over 700 papers can be found online database of U.S. National Library of Medicine in December, 2010.

From engineers' point of view, DECT is a problem of how effectively to use the X-ray spectral information for better diagnosis of various diseases. However, the spectral information lies in the difference between two low and high energy images, so that it is difficult to acquire the accurate spectral information due to amplification of error or noise in the resulting difference images. In this work, a new model and a new technique for DECT image enhancement are proposed to overcome this problem. The proposed technique is based on the fact that the X-ray attenuation of a high density material decreases relatively faster than that of a low density material as X-ray energy increases. This fact has been ignored in most of the DECT techniques. In the following chapters, the basic theory of DECT is reviewed, and the new model and technique for DECT are presented after the discussion of noise characteristics of DECT. Finally, the proposed method is verified with the phantom and real patient studies. And some DECT issues which are related to this work are also discussed.

CHAPTER 2

THEORY OF DUAL-ENERGY CT

2.1 CT as Density Imaging

X-ray imaging measures the attenuation of incident x-ray after passing through a material. The attenuation is quantified as a linear attenuation coefficient μ, which is defined as

$$I = I_0 \exp(-\mu l), \tag{1}$$

where I_0 is the X-ray source intensity and I is the intensity at the detector after passing through a homogenous material of a length l. The linear attenuation coefficient is obtained directly by taking the minus log to Eq. (1) as

$$\mu = -\frac{1}{l}\log(I / I_0). \tag{2}$$

Computed tomography (CT) is a tomographic representation of X-ray attenuation of body tissues. For the ideal monochromatic X-ray source and an inhomogeneous object, the attenuation model becomes

$$I = I_0 \exp\left(-\int \mu(\mathbf{r})dl\right), \tag{3}$$

where $\mathbf{r} = (x, y, z)$ is the spatial position vector and $\int \mu(\mathbf{r})dl$ is the line integral over the X-ray path. The projection measurement p is defined as the minus log ratio of source and measurement intensity as

$$p = -\log(I / I_0) = \int \mu(\mathbf{r})dl. \tag{4}$$

In CT imaging, the spatial distribution of $\mu(x, y, z)$ is recovered from the projection measurements p of Eq. (4) acquired over 360° scanning, and a typical CT machine reconstructs one slice image of a 512×512 matrix size from over one million projection data. There are several CT reconstruction methods such as the filtered back-projection, algebraic reconstruction, and iterative reconstruction. All the methods try to uncover the spatial distribution of $\mu(x,y,z)$ from the projection measurements p. The filtered back-projection is a standard CT reconstruction method for its speed and accuracy [50]. Developing CT reconstruction method requires intense mathematical formulation and rigorous efforts and is one of major research topics in CT imaging. This work aims to enhance and take advantage of the reconstructed dual-energy CT (DECT) images and so only the reconstructed μ is considered.

Generally, the linear attenuation coefficient μ depends on X-ray energy, the density ρ (g/cm^3), effective atomic number $\hat{Z}$ of the material as

$$\mu = u\left(E, \hat{Z}\right) \cdot \rho, \tag{5}$$

where u is the mass attenuation coefficient (cm^2/g). Normally, the X-ray attenuation of a material is measured for its homogeneous medium and is normalized by material density, and it is called the mass attenuation coefficient of the material. National Institute of Standards and Technology (NIST), USA provides the tabulated standard data of mass attenuation coefficients of various elementary media and compound mixtures.

In a typical X-ray energy ranges of CT imaging, the density is the dominant factor of contrast [50] and so μ becomes simplified as

$$\mu = u\left(E\right)\rho. \tag{6}$$

In CT imaging, this linear attenuation coefficient μ of a material is presented relative to that of water μ_{water}, and so-called CT number P is defined as

$$
\begin{aligned}
P &= \frac{\mu - \mu_{water}}{\mu_{water}} \times 1000 \\
&= \left(\frac{\mu}{\mu_{water}} - 1 \right) \times 1000 \qquad \text{(HU)}.
\end{aligned}
\tag{7}
$$

It is specified in Hounsfield units (HU) in honor of the inventor of CT, and water has 0 HU and air has around -1000 HU [50] by definition.

The physical meaning of CT number becomes clear with the relation of Eq. (6). Since $\mu = u(E)\rho$ and $\mu_{water} = u_{water}$ (ρ_{water} =1g/cm^3) and if $u \approx u_{water}$, the equation (7) becomes

$$
\begin{aligned}
P &= \left(\frac{u}{u_w} \rho - 1 \right) \times 1000. \\
&\approx (\rho - 1) \times 1000 \quad if\, u \approx u_{water}.
\end{aligned}
\tag{8}
$$

Most body tissues except bone and lung tissue have attenuation similar to water attenuation and so the CT value directly represents material density (1 HU $\approx$ 1 g/cm^3). Therefore, CT can be considered as density imaging, which is an advantage of CT over MRI (Magnetic Resonance Imaging). MRI has several imaging parameters such as echo time, repetition time and inversion time. The different combination of these MR imaging parameters produces images different in physical sense, which ironically makes it difficult for radiologists to interpret the physical meaning of MRI images without careful consideration of the applied parameters. Contrary to this, the interpretation of CT images is straight-forward, density imaging, which is one of advantage of CT imaging over MRI.

2.2 The Limitation of Conventional CT imaging

In CT imaging, X-ray source is polychromatic and the target material is inhomogeneous, so that the simple polychromatic X-ray attenuation model of Eq. (3) is not valid in real situation.

The general model for the polychromatic X-ray source and an inhomogeneous object is given as,

$$I = \int I_0(E) \exp\left[-\int \mu(\mathbf{r}, E) dl \right] dE, \tag{9}$$

where the linear attenuation coefficient μ is expressed as a function of the spatial position $\mathbf{r} = (x, y, z)$ and X-ray energy E, and $\int \mu(\mathbf{r}; E) dl$ is the line integral over the X-ray path. And the projection measurement p becomes as

$$p = -\log\left[\int I_0(E) \exp\left[-\mu(\mathbf{r}, E) dl \right] dE / \int I_0(E) dE \right]. \tag{10}$$

However, due to the polychromatic nature of X-ray source, taking log directly as Eq. (10) causes nonlinearity of the line integral, which is known as beam hardening or spectral artifacts of CT imaging and causes cupping, shading, or streaking artifacts in the reconstructed images [50]. This spectral artifact limits the accuracy of attenuation measurement in CT imaging, especially near high-attenuation materials such as bone and metal implants. How to correct this nonlinearity is a typical calibration problem in CT imaging. Using a uniform phantom of known density and geometry, the typical calibration procedure approximates the nonlinear relationship between the projection measurement p and the measured intensity I using power series as

$$p = a_0 + a_1 \log(I) + a_2 \left[\log(I) \right]^2 + \cdots. \tag{11}$$

Stonestrom et al. summarized theories of spectral artifact corrections [4]. They also pointed out that such nonlinearity can be resolved by taking logs first and summing the projection measurement p, the logs over the energy spectrum E_n as

$$\begin{aligned} p &= \frac{1}{N} \sum_{n=1}^{N} -\log\left(\frac{I_n}{I_{0n}} \right) = \frac{1}{N} \sum_{n}^{N} \int \mu(\mathbf{r}; E_n) dl \\ &= \int \bar{\mu}(\mathbf{r}) dl, \end{aligned} \tag{12}$$

where

$$\bar{\mu} = \frac{1}{N}\sum_{n=1}^{N}\mu(\mathbf{r}; E_n). \tag{13}$$

Current X-ray technology cannot obtain the energy spectrum information E_n yet and so this formulation is not feasible in reality. However, one important consequence of this formulation is that the linear attenuation coefficient obtained in CT imaging is actually the average value $\bar{\mu}$ of attenuation over broad spectrum of X-ray energies.

In addition to such artifacts as beam hardening, the major intrinsic limitation of CT imaging is low contrast. The CT number of major body tissues ranges -100 to 100 HU (about 0.9 ~ 1.1 g/cm^3) except bone (> 150 HU) and lung tissue (< -500HU). The density differences of body tissues are too small to differentiate them clearly from each other if it is within 10 HU differences due to the system limitation such detector efficiency, noise, and X-ray radiation safety issue etc. Noise can be reduced by increasing X-ray exposure. However, increasing X-ray radiation is limited due to the patient safety issue for X-ray radiation dose. So, contrast agents are used in routine CT imaging to enhance the contrast difference between abnormal tissues and surrounding tissues. Various organic iodine solutions such Omnipaque, Ultravist and Visipaque are widely used for the contrast agents. Iodine is five times denser (4.93g/cm^3) than water and shows over 20-50 times attenuation in the typical CT X-ray energy range, and so iodine-enhanced and unenhanced tissues become better differentiable through their relative contrast difference.

Besides the noise and low-contrast problem, conventional CT imaging is limited by the fact that different materials can have the similar CT value, which may lead to misdiagnosis or uncertainty. DECT has been reintroduced to solve this problem by using the additional spectral information of tissue attenuations.

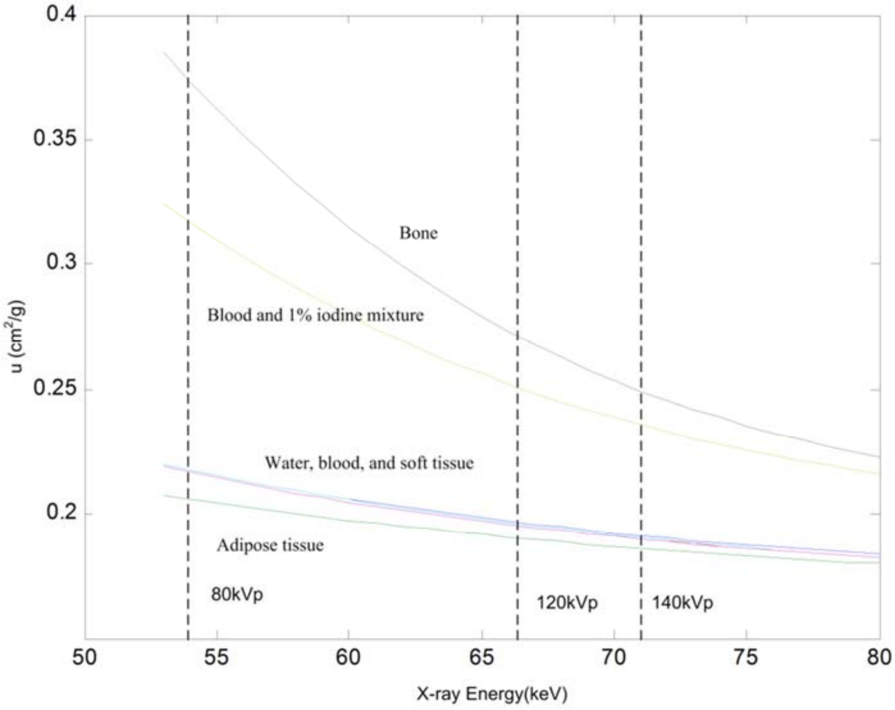

Figure 1. Mass attenuation coefficients over CT x-ray energy range. These plots were calculated using the tabulated data of mass attenuation coefficients of National Institute of Standards and Technology (NIST), USA. The dashed lines are the effective energy of typical 80, 120 and 140kVp CT imaging, which are about 53, 67 and 72keV respectively.

2.3 Dual-Energy CT

Different materials attenuate differently as the incident X-ray energy changes. DECT targets to utilize the energy-dependency of tissue attenuation. The energy dependency of body tissue attenuation was given in Figure 1 over the typical X-ray energy range of CT imaging. Note that the X-ray attenuation of bone is higher and decreases more rapidly than soft tissue attenuation as X-ray energy changes in Figure 1. This different energy dependency can be utilized for tissue characterization.

It is important to note that each X-ray tube voltage produces X-ray of unique effective energy, even though X-ray is polychromatic, so that different X-ray attenuations are acquired for the different X-ray tube voltages. The standard low and high X-ray tube voltages of DECT are 80kVp and 140kVp, of which effective energies are about 53keV and 72eV, respectively (the dash lines in Figure 1), while the effective energy of the standard conventional 120kVp CT imaging is about 67keV. These plots of Figure 1 were calculated using the tabulated data of mass attenuation coefficients of National Institute of Standards and Technology (NIST), USA.

DECT is the problem how to extract the unique information from two X-ray spectral measurements and how to use it for CT image enhancement, accurate density measurement and material characterization. The most straightforward method for CT image enhancement using dual-energy information is weighted average of low and high energy images. In other words, it is a typical image processing problem to combine two images of different information for best signal-to-noise ratio (SNR) or contrast-to-noise ratio (CNR) as

$$P_0 = \alpha P_L + \beta P_H, \tag{14}$$

where P_L and P_H are the reconstructed CT images of low and high X-ray energies, and α and β are the weighting factors ($\alpha + \beta = 1$). This weighted average of two images was adapted as to Siemens DSCT in 2007 [30], in which the so-call virtual 120kVp image is generated as one of default images by weighted averaging of 30% 80kVp and 70% 140kVp images. Note 0.3×80 + 0.7×140=122kVp. The virtual 120kVp is the best SNR in linear combinations of low and high energy images. Although it is not optimal in CNR, the value of the virtual 120kVp image is in that it has similar image characteristics to the standard 120kVp CT images, especially in quantification of tissue [46, 51]. Therefore, DECT results can be compared to those of the standard 120kVp CT imaging with the virtual 120kVp image. With the introduction of DSCT, the blending of low and high energy images in order to produce the best CNR images becomes the one of active topics of DECT. Recently, rather than using linear weighting of two images, Holms et al. reported that non-linear blending using a modified sigmoid function significantly improved CNR over the virtual 120kVp images and the resulting images are preferred by radiologists for visual perception [52].

Depending on how to extract the two X-ray spectral information, DECT approaches for material characterization can be classified broadly into projection-based methods and image-based methods. Projection-based methods preprocess the projection data to extract energy-independent information before the reconstruction, while image-based methods utilize the separately-reconstructed low and high images for the spectral application.

The spectral information lies in the difference between the low and high energy images. So the most direct method to acquire the spectral information is the weighted subtraction of two images. This method is mainly used in dual-energy subtraction digital radiography [53-55] and dual-energy X-ray absorptiometry [56]

The projection-based method is preferred for two-material decomposition, which is mainly attributed to the rigorous formulation of Alvarez and Macovski [7]. They originally proposed decomposition of the linear attenuation coefficient μ of an unknown material into the components of photoelectric absorption f_p and Compton scatter f_c, which are the major two X-ray interactions in diagnostic energy region. The photoelectric effect and Compton scatter are the mutually exclusive X-ray interaction. In other words, they can be expressed by mathematical functions independent to each other. Therefore, the decomposition is mathematically modeled as

$$\mu(E) = c_p f_p(E) + c_c f_c(E), \tag{15}$$

where c_p and c_c are the coefficients for photoelectric effect and Compton scattering, respectively. Through this decomposition, the X-ray energy dependency of linear attenuation coefficient of a material is transferred into the tow basis functions of energy, $f_c(E)$ and $f_p(E)$. It is their idea that the c_p and c_c are independent to X-ray energy. They become dependent only to the physical properties of the unknown material such as mass density, the atomic weight and atomic number. Therefore, the coefficients c_p and c_c may be used for material characterization without the beam hardening artifact, which is caused by energy dependency of μ in CT imaging.

Compton-scatter component is estimated by the Klein-Nishina function which is well-known for its accurate representation of Compton scatter. The Klein-Nishina function is given as

$$f_c(\alpha)=\frac{1+\alpha}{\alpha^2}\left[\frac{2(1+\alpha)}{1+2\alpha}-\frac{1}{\alpha}\ln(1+2\alpha)\right]+\frac{1}{2\alpha}\ln(1+2\alpha)-\frac{(1+3\alpha)}{(1+2\alpha)^2} \tag{16}$$

with $\alpha = E/510.975$ keV. On the other hand, no accurate analytical function representing the photoelectric effect is known. So the photoelectric basis is estimated empirically as

$$f_p=\frac{1}{E^3}. \tag{17}$$

With Compton scatter and photoelectric decomposition model, the system equations for DECT become as

$$\begin{gathered} I_L(A_1,A_2)=\int I_{0L}(E)\exp\left[-\left(A_1 f_p(E)+A_2 f_c(E)\right)dl\right]dE \\ I_H(A_1,A_2)=\int I_{0H}(E)\exp\left[-\left(A_1 f_p(E)+A_2 f_c(E)\right)dl\right]dE \\ A_1=\int c_p(x,y)\,dl \quad \text{and} \quad A_2=\int c_c(x,y)\,dl. \end{gathered} \tag{18}$$

The projection-based method targets to obtain the two transmission line integrals of A_1 and A_2. For a monochromatic X-ray source, the system equations of Eqs (18) can be simplified as

$$\begin{aligned} p_L &= -\log\left[I_L\left(A_1, A_2\right) / I_{0L}(E_L) \right] = A_1 f_p\left(E_L\right) + A_2 f_c\left(E_L\right) \\ p_H &= -\log\left[I_L\left(A_1, A_2\right) / I_{0H}(E_H) \right] = A_1 f_p\left(E_H\right) + A_2 f_c\left(E_H\right). \end{aligned} \tag{19}$$

However, this monochromatic X-ray source is infeasible in practice. Therefore, for a typical polychromatic X-ray source, it becomes a non-linear problem to solve the following system equations for A_1 and A_2

$$\begin{aligned} p_L &= -\log\left[\int I_{0L}(E)\exp\left[-\left(A_1 f_p(E) + A_2 f_c(E)\right)dl\right]dE \,/ \int I_{0L}(E)dE \right] \\ p_H &= -\log\left[\int I_{0H}(E)\exp\left[-\left(A_1 f_p\left(E\right) + A_2 f_c\left(E\right)\right)dl\right]dE \,/ \int I_{0H}(E)dE \right] \end{aligned} \tag{20}$$

The system equations (20) are approximated by the power series or polynomial functions. In practice, the mapping functions from the projection measurements p_L and p_L to the transmission line integral A_1 and A_2 are predefined for various ranges of A_1 and A_2 values by experimental calibration as

$$\begin{aligned} A_1 &= a_0 + a_1 p_L + a_2 p_H + a_3 p_L p_H + a_4 {p_L}^2 + a_5 {p_H}^2 + \cdots \\ A_2 &= b_0 + b_1 p_L + b_2 p_H + b_3 p_L p_H + b_4 {p_L}^2 + b_5 {p_H}^2 + \cdots. \end{aligned} \tag{21}$$

Once the line integral sets of A_1 and A_2 are obtained, the spatial distributions of Compton scattering coefficient c_c and photoelectric effect coefficient c_p are reconstructed using a CT reconstruction method and are used for material characterization.

This Compton scatter and photoelectric decomposition was generalized later into two-material decomposition by Lehmann et al. [57]. They showed that the Compton scatter and photoelectric absorption components can be integrated into the mass attenuation coefficients u of two known materials which have very different X-ray energy dependency. The combination of mass attenuation coefficients of two distinct materials is mathematically equivalent to the linear combination of Compton scatter and photoelectric effect. Therefore, the linear attenuation coefficient of any material can be expressed directly by mass attenuations two basis materials as

$$\mu\left(E\right)=u_1\left(E\right)\cdot m_1+u_2\left(E\right)\cdot m_2, \tag{22}$$

where the subscript indicates the basis material and m_i has a dimension of density (g/cm^3). Physically, the densities m_1 and m_2 are the equivalent amounts of the two basis materials to produce the same X-ray attenuation of the unknown material. In this two-material decomposition, the pair of two-equivalent densities of the basis materials is the unique information which characterizes the unknown material as Compton-scatter and photoelectric decomposition does.

The projection-based procedure of Eq. (22) for the two-material decomposition is the same as the Compton-photoelectric decomposition. Only the definitions of line integrals of A_1 and A_2 are changed and the basis sets are replaced with u_1 and u_2 as

$$A_1=\int m_1\left(x,y\right)dl \quad \text{and} \quad A_2=\int m_2\left(x,y\right)dl, \tag{23}$$

and the system equations become as

$$\begin{aligned} p_L &= -\log\left[\int I_{0L}(E)\exp\left[-\left(A_1u_1(E)+A_2u_2(E)\right)dl\right]dE \,/ \int I_{0L}(E)dE\right] \\ p_H &= -\log\left[\int I_{0H}(E)\exp\left[-\left(A_1u_1\left(E\right)+A_2 f_2\left(E\right)\right)dl\right]dE \,/ \int I_{0H}(E)dE\right]. \end{aligned} \tag{24}$$

And the mapping functions of Eqs. (21) are prepared for the various density values of the two basis materials. One of the advantages of this two-material decomposition over Compton-photoelectric decomposition is the easiness of calibration. The attenuation functions of two basis materials are readily obtainable through NIST or experiments, and the resulting equivalent densities are easily understandable and used for the tissue characterization than Compton scattering and photoelectric components. So, two-material decomposition model of Eq. (22) is practically preferred to Compton-scatter and photoelectric decomposition in the recent projection-based DECT applications. Compton scatter and photoelectric decomposition is mainly used to provide the theoretical backgrounds of DECT nowadays.

Once the equivalent material densities m_1 and m_2 of basis materials are acquired, the attenuation function $\mu(E)$ of the unknown material can be approximated over broad X-ray energy ranges, and so pseudo-monochromatic image can be generated at a chosen X-ray energy level E from the relation of Eq. (22). The pseudo-monochromatic imaging has been implemented as Gemstone spectral imaging of Discovery CT750HD, GE in 2009. In the Gemstone spectral imaging, the attenuation plots of target regions of interest (ROI) are displayed and compared over broad X-ray energy ranges [2]. The pseudo-monochromatic image was expected to produce the image free of beam hardening artifacts. However, any successful result of beam hardening correction for clinical images using pseudo-monochromatic image has not been shown yet.

Although the projection-based method is mainly used for material decomposition, it can be done directly using reconstructed images. Hawkes et al. [58] proposed in 1986 that the X-ray attenuation of tissue can be expressed in the mixture of two basis materials directly using the reconstructed low and high energy images. They formulated the direct relationship between CT value of the reconstructed image and equivalent densities of Eq. (22) as

$$P = 1000(m_w - 1) + m_I \phi_I , \tag{25}$$

where m_w and m_I are the dimensionless coefficients of basis materials such as water and iodine, and $\phi_I = u_I / u_w$. They formulated Eq. (25) from the definition of CT number P of Eq. (7). Note that the equation (25) is obtained by normalizing equation of (26) by one of basis material. They also characterized various materials including body tissue such as liver, muscle, spine and etc. with the coefficient m_I . One of advantages of this approach over the projection-based material decomposition is the easiness of calibration.

Although the projection-based and image-based two-material decomposition appear different, either the projection-based method or the image-based method is basically the same problem to solve the system equations,

$$\begin{aligned} \mu_L &= u_{L1} m_1 + u_{L2} m_2 \\ \mu_H &= u_{H1} m_1 + u_{H2} m_2 , \end{aligned} \tag{26}$$

for the equivalent density values m_1 and m_2 . Only calibration or the treatment for the nonlinearity of Eq. (10) or (24) to recover μ from the projection measurements makes the difference.

The meaning of material decomposition becomes clear in vector representation. Two measurements of linear attenuation coefficients of low and high X-ray energy constitute a vector $\mathbf{x} = (\mu_L, \mu_H)$. In the vector representation of Figure 2, $\mathbf{u}_1 = (\mu_{L1}, \mu_{H1})$ is the water basis and $\mathbf{u}_2 = (\mu_{L2}, \mu_{H2})$ is the iodine basis. A material whose attenuation decreases faster than water as X-ray energy increases locates within the two basis vector like A, and a material whose attenuation decreases slower than water locates outside like B in Figure 2. For examples of clinical imaging, contrast enhanced liver tissues are the former A, and fatty tissues are B, in Figure 2. It is important to notice that the equivalent density of the iodine basis for fatty tissue B is negative ($b_2 < 0$ in Figure 2), which appears physically non-sense. However, the material decomposition is a mathematical representation of the equivalent amounts of the two basis materials, which produce the same X-ray attenuation of the unknown material, so that the equivalent density can be a negative value. Although it is

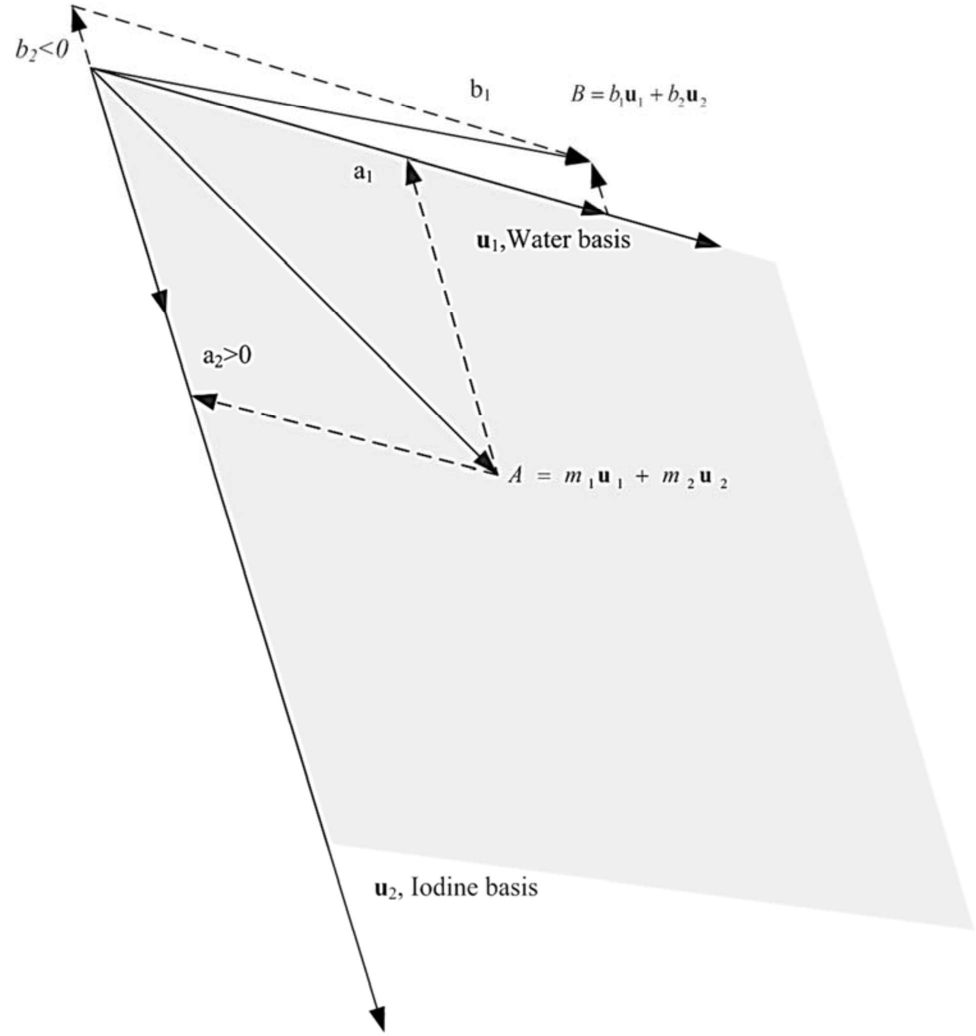

Figure 2. Material decomposition of DECT. $\mathbf{u}_1$ is the water basis and $\mathbf{u}_2$ is the iodine basis. A material which attenuates faster as x-ray energy changes than water will locate within the positive direction (gray region) of the two basis vectors like *A*, and a material which attenuates slower than water will locate outside like *A*. It is important to notice that the equivalent density b_2 of iodine for *B* is negative ($b_2 < 0$). In clinical imaging, contrast enhanced liver tissues are the former *A*, and fatty tissues are the later *B*.

straightforward to engineers, radiologists need to be aware of it in interpretation of the resulting density maps.

With DSCT, Siemens introduced a new image-based technique, so-called three-material decomposition [30], in which the CT number pairs of low and high energy images are mapped onto the two-dimensional scatter plot of the CT number diagram of low vs. high energy images. The material or its composition is characterized by the relative position to the pre-defined CT value pairs of fat, soft tissue and iodine in the plot, and the virtual-non contrast image or iodine-content-overlaid image is generated from the decomposition. Basically, it is the same as the vector approach of Figure 2, in which the relative position in the water and iodine space characterizes the material. Only the reference is different.

Another one of interesting methods is the so-called dual-energy index, which is defined as

$$U = \frac{\mu_L - \mu_H}{\mu_L + \mu_H}. \tag{27}$$

Using the CT numbers P_L and P_H of reconstructed images and with the CT number definition of Eq. (7), the dual-energy index is expressed equivalently as

$$U = \frac{P_L - P_H}{P_L + P_H + 2000}. \tag{28}$$

In simulation, this dual-energy index is in the unique and monotonic relation to the effective atomic number of material up to $\hat{Z} = 55$, and so it may be used for material characterization [59, 60]. However, the dual-energy index method has not shown its effectiveness in clinical DECT application yet except the detection of the urinary [2].

In summary, several methods have been proposed for DECT processing and application. The DECT applications of all the methods discussed previously are practically limited by amplifying noise issue, because the spectral information lies in the difference between the two spectral measurements or the two reconstructed CT images of low and high X-ray energies. Any subtraction of two measurements statistically amplifies the noise or errors [61, 62]. To overcome this problem, a new model and a new technique for DECT image enhancement are proposed after the discussion of noise characteristics of DECT in the next chapter.

CHAPTER 3

DUAL-ENERGY CT IMAGE ENHANCEMENT

Dual-energy computed tomography (DECT) utilizes two X-ray spectral information of body tissue attenuation and aims for accurate density estimation and material differentiation. By combining low and high energy images of DECT, we can estimate density values more accurately because the noise tends to be canceled out in summation. The so-called virtual 120kVp of DSCT is the case that the image quality is improved by blending of 80kVp and 140kVp images. More importantly, the virtual 120kVp image is comparable to the standard 120kVp CT image in the aspect of quantification of regions of interest (ROI) [63]. However, the improvement of image quality can be achieved even in the conventional CT imaging just by increasing the radiation dose.

The real value of DECT is to utilize the spectral information of tissue attenuation, which lies in the difference between low and high energy images P_L and P_H or measurements as

$$\Delta P = P_L - P_H. \tag{29}$$

Any image subtraction statistically elevates the noise level in the resulting difference image and also tends to magnify measurement errors. So, we have to extract the spectral information among this difference deteriorated by noise or error. Therefore, any DECT processing to utilize the spectral information requires an efficient noise suppression technique. All the noise suppression techniques for DECT target to reduce noise without loss of edge details and diagnostic information.

The correlated noise reduction is one of the popular methods for dual-energy X-ray imaging. It was originally proposed by Kalender *et al.* [62]. It is based on the finding that the noises of density maps m_1 and m_2 of two-material decomposition are negatively correlated and can be balanced on the reference attenuation. Its effectiveness on noise suppression without much loss of quantitative information and detail has been shown [61]. In addition to the anticorrelated relationship of density maps, DECT processing can further exploit the expected trend that the attenuation of high-density materials decreases relatively faster than low-density materials as X-ray energy increases, which has been ignored in most of DECT processing.

Recently, I proposed a simple noisy detection scheme by identifying the spectral error, which is a pixel pair of low and high energy images that deviates far from the expected attenuation trends of body tissues in DECT. After discussing the tissue attenuation trends and analyzing the spectral-error sources of DECT images, a new technique for DECT to improve material differentiation as well as image quality of SNR and CNR is proposed. It consists of three steps: water-reference offset correction, spectral-error correction, and KCNR. Next, the tissue attenuation trend over X-ray energy change is discussed.

3.1. Dual-Energy CT Model and Spectral Error

Typical patterns of DECT measurements are shown schematically in Figure 3. All the CT value pairs of 80kVp and 140kVp images have the same value at the virtual 120kVp but show different energy dependency of attenuations in Figure 3. This is exactly the problem of conventional CT imaging that different materials can have the similar CT number.

The conventional standard CT imaging acquires only the attenuation at 120kVp and so all the attenuations A-E of Figure 3 represent the same material in the conventional 120kVp CT imaging. In Figure 3, DE acquisition of the attenuation information at both 80kVp and 140kVp reveals that they are different materials. However, the attenuations A-E can be the compromised measurements of the same material due to noise or error, then it is questioned which one is the true attenuation of the material. Without any priori-knowledge of material

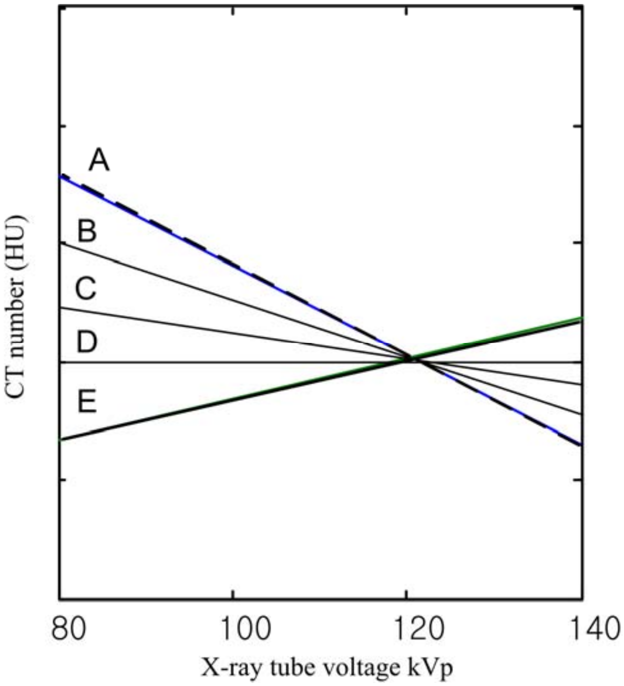

Figure 3. Typical patterns of DECT images. All the pixel pairs of 80kVp and 140kVp have the same CT number at the 120kVp but show different energy dependencies of attenuations. Without any priori-knowledge of the material, it is difficult to determine which one is true attenuation or error over X-ray energy change.

attenuation, it is impossible to determine which one is the true attenuation of the material over energy. This work provides a priory-knowledge for the material attenuations in DECT imaging.

Figure 4 shows the mass attenuation coefficients *u* of major body tissues and their corresponding CT-number changes over the typical X-ray energy range of CT imaging. Generally speaking, the attenuation of high density materials decreases more rapidly than low density materials, as X-ray energy increases. For example, the attenuation of fatty tissue decreases slower, but those of other heavy tissues such as blood and soft tissue decrease faster relative to that of water as X-ray energy increases. These trends become more obvious in the contrast-enhanced CT imaging. The iodine has high density and its X-ray attenuation decreases more rapidly than that of water, whereas fatty tissue attenuation decreases more slowly than that of water as X-ray energy increases. This relationships is mathematically expressed as

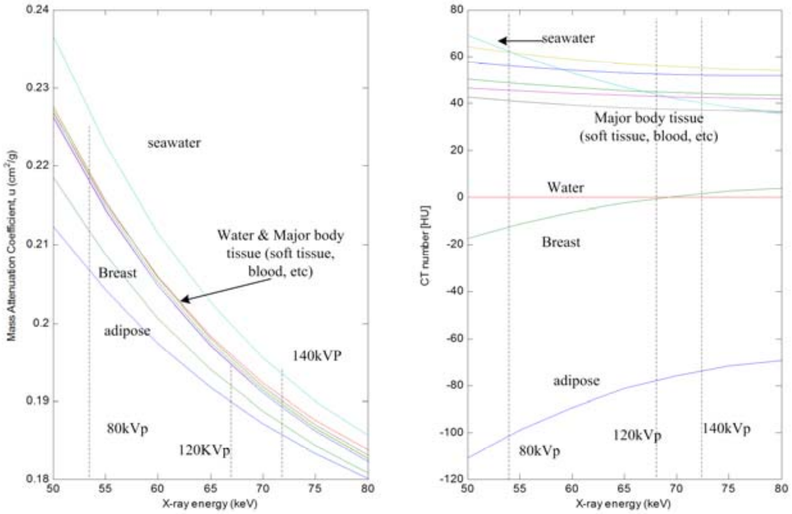

Figure 4. Mass attenuation coefficients u and CT numbers of major body tissues. The u of fatty tissue decrease slower but u of other heavy tissues such as blood and soft tissue decrease faster relative to that of water as X-ray energy increases, and so the CT number of fatty tissue increases ($P_L < P_H$), but that of the heavy tissue deceases $P_L > P_H$.

$$\left|\frac{du_{iodine}}{dE}\right| \gg \left|\frac{du_{water}}{dE}\right| > \left|\frac{du_{fat}}{dE}\right|. \tag{30}$$

Given the attenuation of a reference material μ_0, DECT attenuation trends are expected as,

$$\begin{aligned} \frac{\mu_L}{\mu_{0L}} &> \frac{\mu_H}{\mu_{0H}} \quad if \quad \rho > \rho_0 \\ \frac{\mu_L}{\mu_{0L}} &\approx \frac{\mu_H}{\mu_{0H}} \quad if \quad \rho \approx \rho_0 \\ \frac{\mu_L}{\mu_{0L}} &< \frac{\mu_H}{\mu_{0H}} \quad if \quad \rho < \rho_0, \end{aligned} \tag{31}$$

and then, the expected relationships of Eqs. (31) become simplified to

$$(\rho - \rho_0) \cdot \left(\frac{\mu_L}{\mu_{0L}} - \frac{\mu_H}{\mu_{0H}} \right) \geq 0. \tag{32}$$

In CT imaging, water is the reference material. Since the CT number P is the attenuation normalized by water attenuation, $P = (\mu / \mu_{water} - 1) \times 1000.$

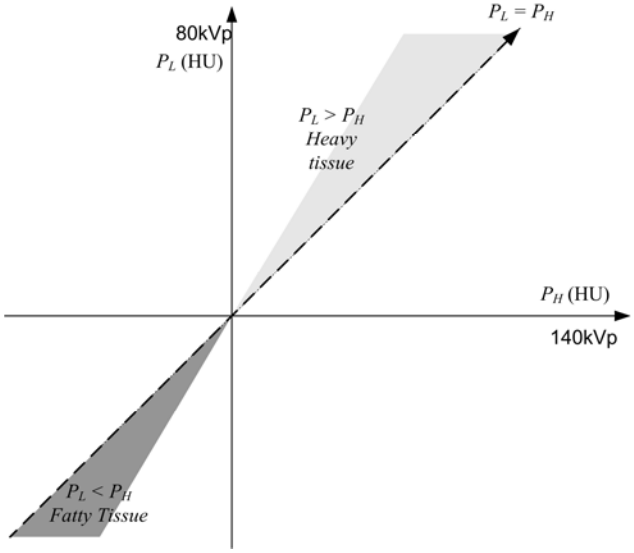

Figure 5. The expected trend of pixel pairs of DECT images in tissue signature plot. The attenuation of high density materials such as iodine and bone decreases faster than that of water as x-ray energy increases, but those of low density materials such as fatty tissues decrease slower so that we can set up a model for the expected trend like Eq. (32) or Eq. (34).

Therefore, with the reconstructed images P_L and P_H , the relationships of Eqs, (31) and (32) can be directly expressed as

$$\begin{aligned} P_L > P_H \quad & if \quad \rho > \rho_w \\ P_L \approx P_H \quad & if \quad \rho \approx \rho_w \\ P_L < P_H \quad & if \quad \rho < \rho_w, \end{aligned} \tag{33}$$

and

$$P_0 \cdot \left(P_L - P_H\right) \geq 0. \tag{34}$$

Note that the virtual 120kVp image P_0 was used in Eq. (34) for the density reference since $P = (\rho - 1) \times 1000$ for $u \approx u_{water}$ [see Eq. (8)]. The virtual 120kVp image has low noise and the similar quantification ability to the true 120kVp image, of which accuracy of density estimation is well established in CT community. Therefore, the virtual 120kVp is a reasonable choice for the density reference of Eq. (32). It is expected that the CT number of fatty tissue increases, but those of heavy tissues decease as X-ray energy increases, and such trends are already shown in the right plot of Figure 4. The DECT attenuation model of Eq.

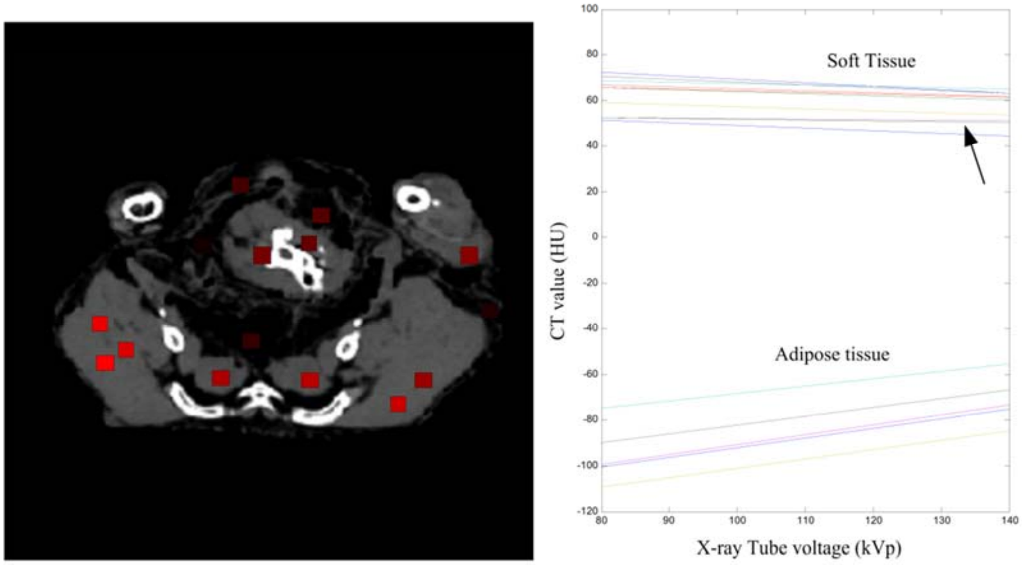

(a) (b)

Figure 6. Phantom study for CT value change over x-ray energy. (a) Chicken meat phantom image. (b) CT values over x-ray tube voltage changes. Two images of 80kVp (300mAs) and 140kVp (193mAs) were acquired separately, and the average CT values of soft tissue and adipose tissue were measured in 15 regions over 5x5 pixels, which were indicated as squares in figure (a). Their CT values were plotted over x-ray tube voltage changes. As expected, the CT values of soft tissues decreased and those of adipose tissues increased at 140kVp. Note that some soft tissues changed little (arrow). However, it is due to the calibration error (see text for discussion).

(34) predicts 80kVp and 140kVp CT-value pairs to be distributed like tissue signature plot of Figure 5.

In order to verify the model of Eq. (34), phantom imaging of whole chicken meat was performed at 80kVp (300mAs) and 140kVp (193mAs) separately with 0.675mm slice thickness using GE LightSpeed VCT. Note that this phantom imaging was performed in ideal DECT imaging condition; no misregistration and good X-ray exposure because of the small size of the phantom and high tube currents. The average CT values of 15 samples of soft tissue and adipose tissue were measured over 5×5 pixel regions which are pointed as squares in Figure 6a. Note that CT values of soft tissue decrease and those of adipose tissues increase at 140kVp (Figure 6b). Some soft tissues attenuated like water and showed little change in their CT values (arrow in Figure 6b).

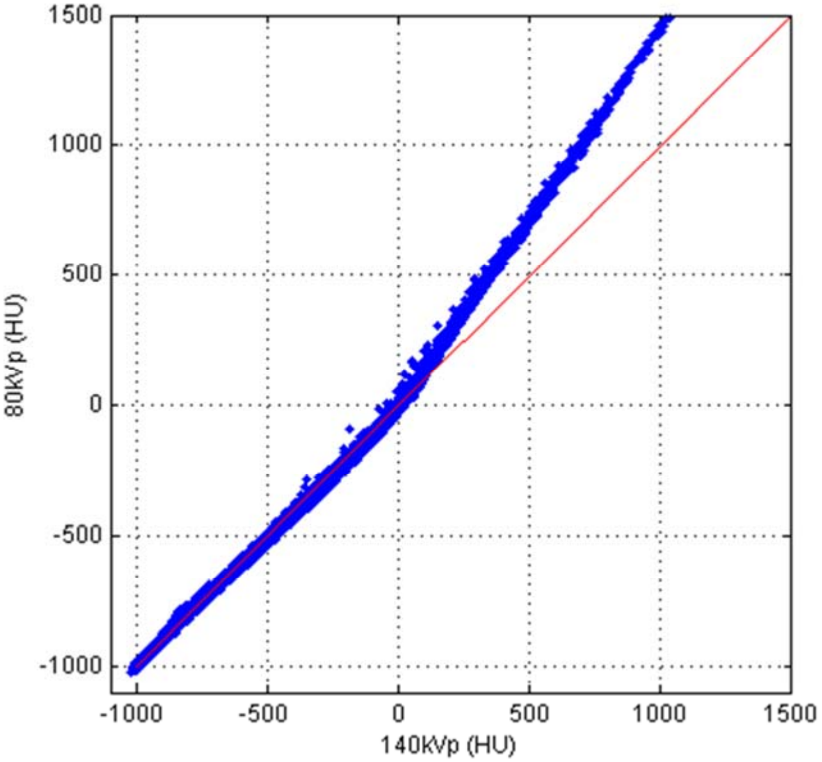

Figure 7. Tissue Signature Plot (80kVp vs. 140kVp) of the Chicken meat phantom. The solid line is for the pixel pairs, where CT values are the same at 80kVp and 140kVp ($P_L = P_H$). Note that the most of fatty tissues positioned in lower and soft tissue in higher than the solid line as the model of Eq. (34).

It was questioned whether the water-like attenuations (arrow in Figure 6b) are the property of the tissues or due to a calibration error. In most of the phantom studies, CT values of the water reference were biased negatively at 80kVp sometime over -10 HU and somewhat less at 140kVp, even though system calibrations were performed before each imaging.

The decreasing trend of heavy density materials became more obvious with the correction of such a bias using the water reference included in phantom imaging. However, the water reference was not included in this chicken meat phantom imaging of Figure 6. DECT utilizes the energy dependency of tissue attenuation so that any bias in low and high energy

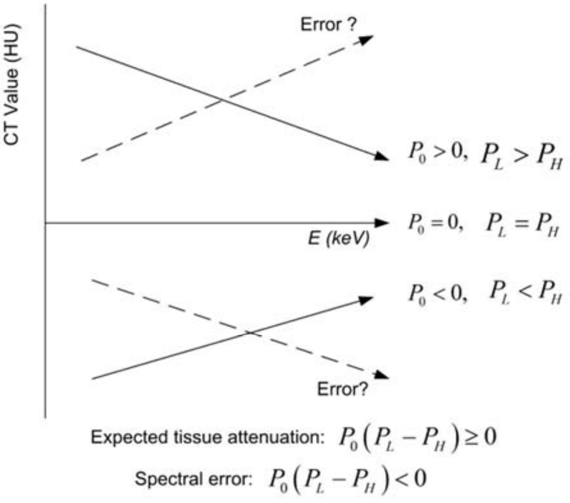

Figure 8. DECT spectral error

images will cause severe problems in DECT applications. The water-like attenuation of soft tissues in the chicken meat phantom imaging was mainly due to the calibration error. How the attenuations of this chicken-meat phantom change after the post-calibration algorithm is applied is shown in Figure 17b.

The tissue signature plot (80kVp vs. 140kVp) of chicken-meat phantom images shows the expected trends in Figure 7, where the solid line represents the pixel pairs which have the same CT number at 80kVp and 140kVp, ($P_L = P_H$). The iso-line represents any attenuation parallel to that of water in vector space representation of Figure 2. Most of fatty tissues positioned in lower, but soft tissue positioned in higher than the solid line as the model of Eq. (34) predicted.

Therefore, any pixel-pair of low and high energy CT that deviates far from this expected trend of Eq. (34) can be considered as noise or error, and so the condition of an error pixel is

$$P_0 \cdot \left(P_L - P_H\right) < 0. \tag{35}$$

This error is called the ***spectral error*** of DECT [64] and is represented schematically in Figure 8. Figure 9 shows the pixels of spectral errors in the patient DECT images which were detected through the proposed model of Eq. (35). The images (a) and (b) are the original 80kVp and 140kVp images. The image (c) shows the pixels which satisfy the expected trend of Eq. (34), but the image (b) is the pixels of spectral error of Eq. (35). Most

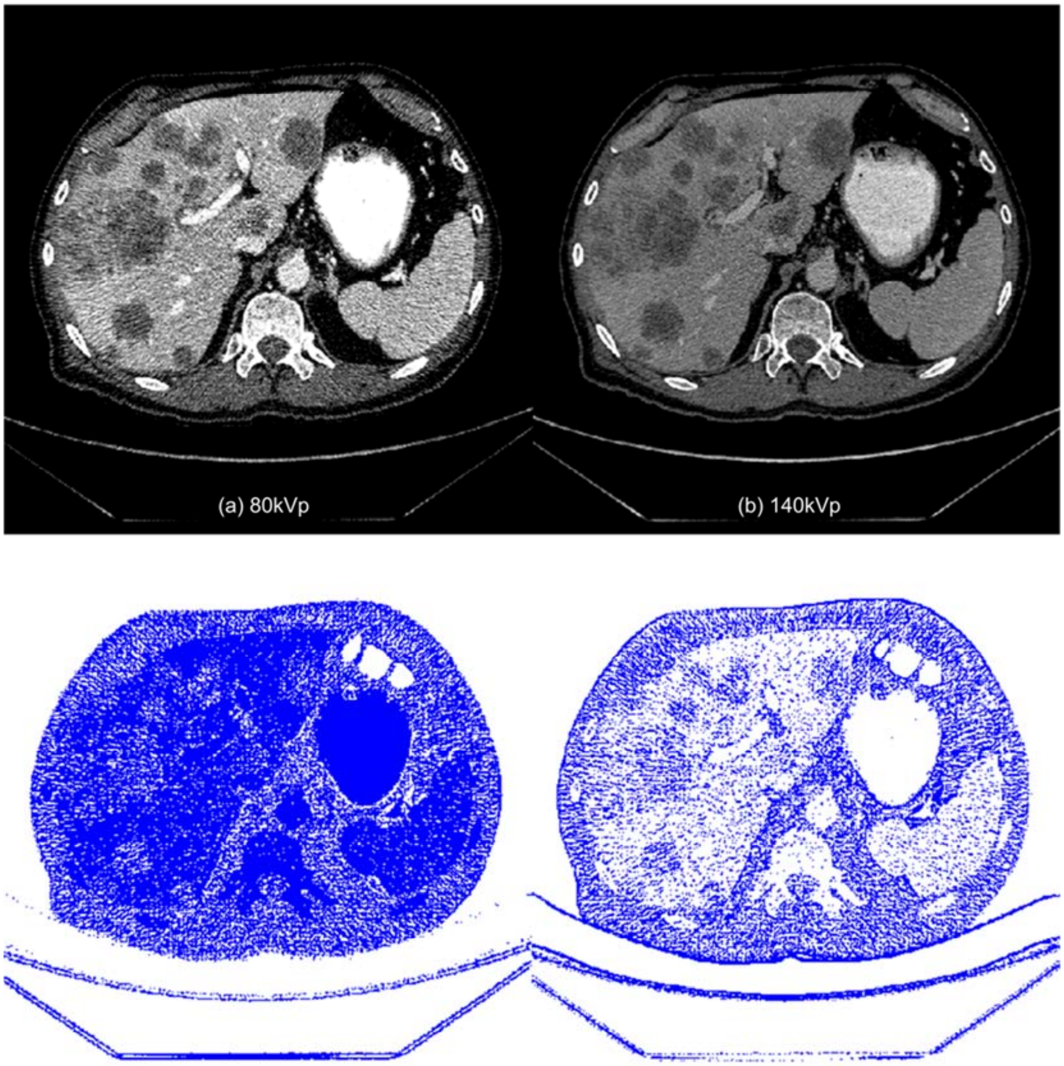

(c) $P_0\left(P_L - P_H\right) \geq 0$

(d) $P_0\left(P_L - P_H\right) < 0$

Figure 9. The pixels of spectral error in DECT patient images. The images (a) and (b) are the original 80kVp and 140kVp images, respectively. The image (c) shows the pixels which satisfy the expected trend, $P_0 \cdot \left(P_L - P_H\right) \geq 0.$ but (b) is the pixels of spectral error, $P_0 \cdot \left(P_L - P_H\right) < 0.$

of spectral errors are in the adipose tissue, soft tissue or liver lesions. All the pixels of the spectral error in Figure 9c clearly show most of anatomical and morphological features of the abdomen. In Figure 9, even the pixels of the homogenous patient-supporting bed show up in both (c) and (d). Statistically, it is because of uncertainty in representation of the feature.

The tissue signature plot of the patient images of Figure 10a and 10b were presented in

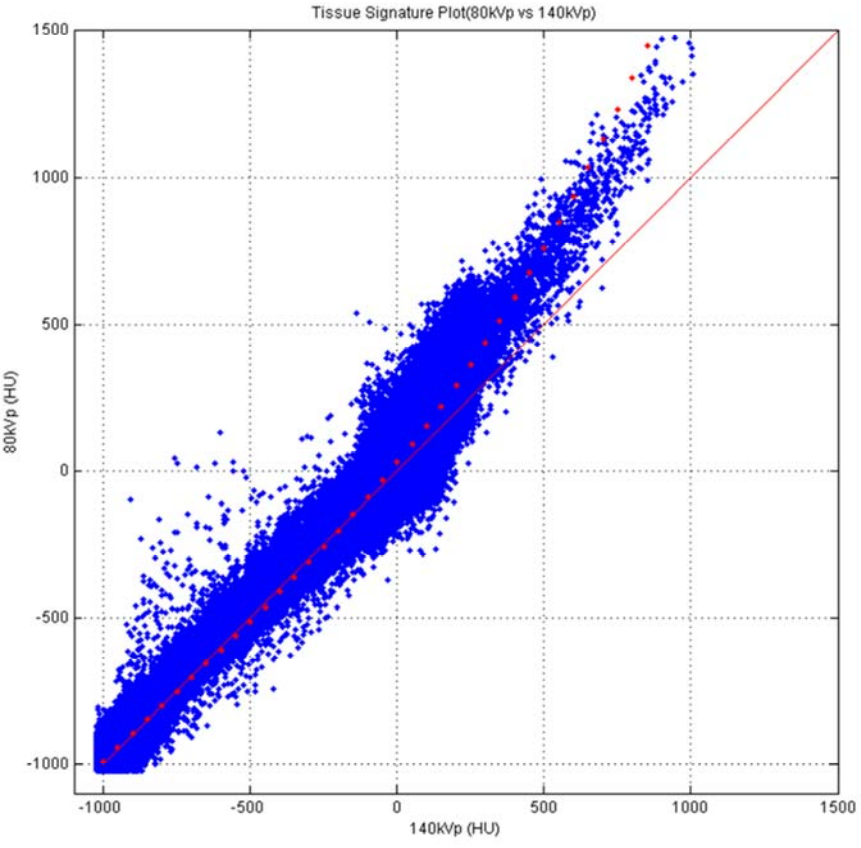

Figure 10. Tissue signature plot (80kVp vs. 140kVp) of the DECT patient image. This is the scatter plot of Figure 8a and b. This scattering plot is far deviated from the expected trend of Figure 6 which was acquired in ideal imaging condition of no misregistration and good X-ray exposure. The solid line is for the pixel pairs, where CT values are the same at 80kVp and 140kVp ($P_L = P_H$).

Figure 9 for the comparison to that of the whole chicken meat in Figure 6 which was obtained in the ideal imaging condition, no misregistration and good X-ray exposure.

With this priori-knowledge of tissue attenuation, the uncertainty can be reduced. The model of Eq. (34) or (35) informs that the attenuations of D and E are errors, if the tissue is iodine-enhanced tissue. If the tissue is adipose tissue, then all the attenuations of A-D are errors. It is the virtual 120kVp P_0 that reliably determines whether the tissue is adipose or iodine-enhanced one. The amount of difference between low and high energy images helps to differentiate the tissue type or tissue composite further.

The spectral error causes severe noise or artifacts especially in results of material decomposition or material differentiation. By correcting the spectral error, material differentiation as well as image quality can be improved because the uncertainty due to noise or error is reduced. In the previous work, I showed that even a simple linear-selective filtering on the pixels of spectral error improved signal-to-noise ratio (SNR) and contrast-to-noise ratio (CNR) of liver lesions without much smearing of image details [64]. In this work, more advanced technique is proposed. It consists of three steps: water-reference offset correction, spectral-error correction, and adaptive correlated noise reduction. Each step is based on the property of spectral-error sources of DECT, which is discussed next.

3.2 The Sources of Spectral Error in Dual-Energy CT Imaging

All the error sources of conventional CT imaging such as the beam hardening and partial volume artifacts are still valid to DECT, but the spectral errors are unique to DECT imaging in that all the errors of each low or high energy image show up as the combined effect as spectral error in DECT.

There are three major sources of spectral errors: misregistration, calibration error, and random noise. The misregistration between low and high energy images was the most severe problem in the old DECT systems due to their slow acquisition speed. A typical example of misregistration of patient abdominal DECT images is shown in Figure 9, where the images (c) and (d) are the magnified images of (a) and (b), respectively. The abdominal patient images show misregistration, especially in vessels and lesions. These images were acquired using GE LightSpeed VCT. It was introduced in 2006 and has the features of fast spiral acquisition of 64-detector rows and dual-energy acquisition. Its dual-energy acquisition is performed in two

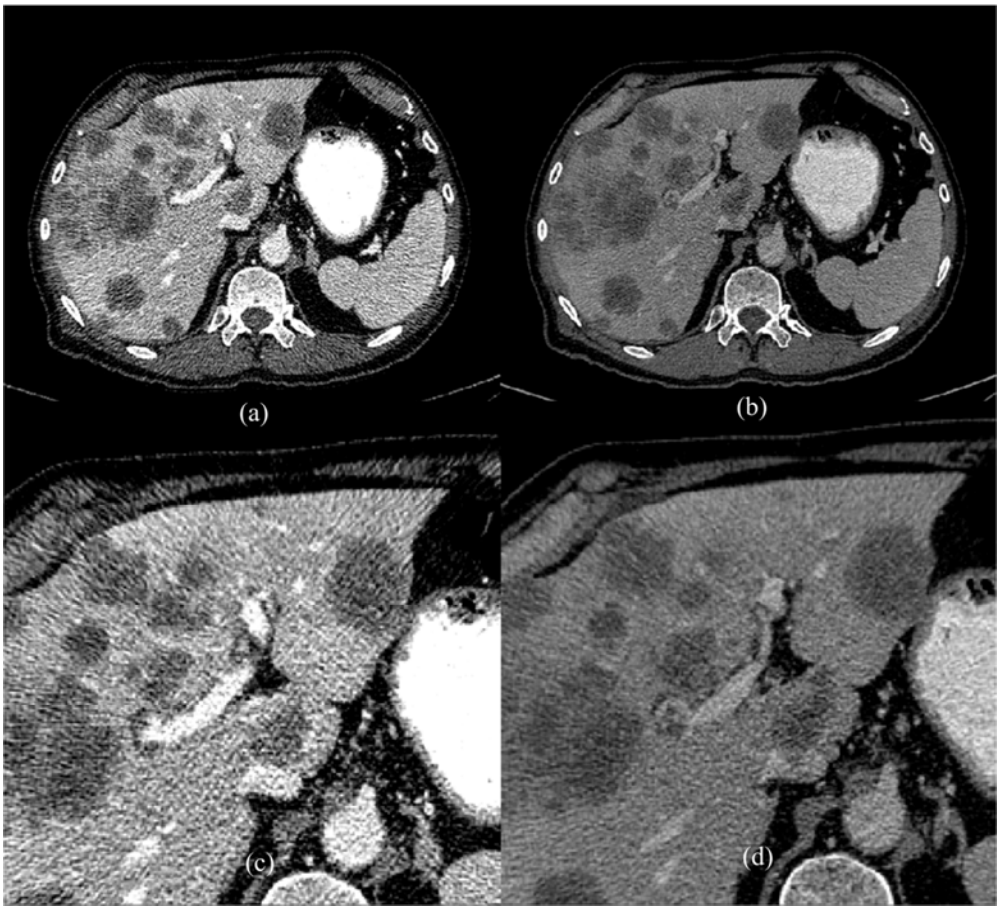

Figure 11. Misregistration of DECT images. Two images of 80kvp (a) and 140kVp (b) show severe misregistration. The images (c) and (d) are the magnified images of (a) and (b). These images were taken using GE LightSpeed VCT, which is an old generation DECT system and acquires two low and high energy images during the two consecutive 0.5-second gantry rotations separated by 0.2 seconds for switching the tube settings.

consecutive 0.5-second gantry rotations separated by 0.2 seconds for switching the tube settings. Obviously, this misregistration will causes errors or artifact in any DECT processing. Recent DECT systems minimized the misregistration problem by fast acquisition using two X-ray sources, a fast voltage-switching tube, or a multilayer detector [2].

Calibration is inherently more important in DECT imaging than conventional CT imaging. In CT imaging, the water is used as a reference material and its CT value must be near 0 HU. Any bias at 80kVp or 140kVp in DECT imaging will distort the energy dependency information of a material. It is presented schematically in Figure 10a. With two low and high energy images which are biased in the same direction, the energy dependency does not change and only the density measurements at 120kVp are affected. However, the different biasing of low and high images causes a large error in the measurement of spectral information. American College of Radiology (ACR) requires the CT value of water reference be within ±7 HU [65]. In the worst case, for an example, if the 80kVp image is biased by 7 HU and the 140kVp image is biased by -7 HU or vice versa, the measured difference will be deviated by 14 HU from the true value of water attenuation. Such attenuations cannot represent water, even though the water reference at virtual 120kVp is the reasonable value of -3.1 HU, and they will show up as contrast-enhanced or fatty tissue in material decomposition. This error can cause severe misdiagnosis in clinical application of DECT. In the DECT analysis of adrenal nodule and metastatic lesions, Gupta et al. [66] reported that the mean attenuation changes from 80kVp to 140kVp were -0.4±7.1 HU for adenomas and -9.2±4.3 HU for metastatic lesions, which means even 10 HU bias in DECT images could lead misdiagnosis of malignant tumors, even though such difference is within acceptable range of conventional CT imaging. Therefore, the accurate calibration of both low and high energy imaging is more important in DECT than the conventional CT imaging, and the accurate measurement of energy dependency using DECT is more challenging.

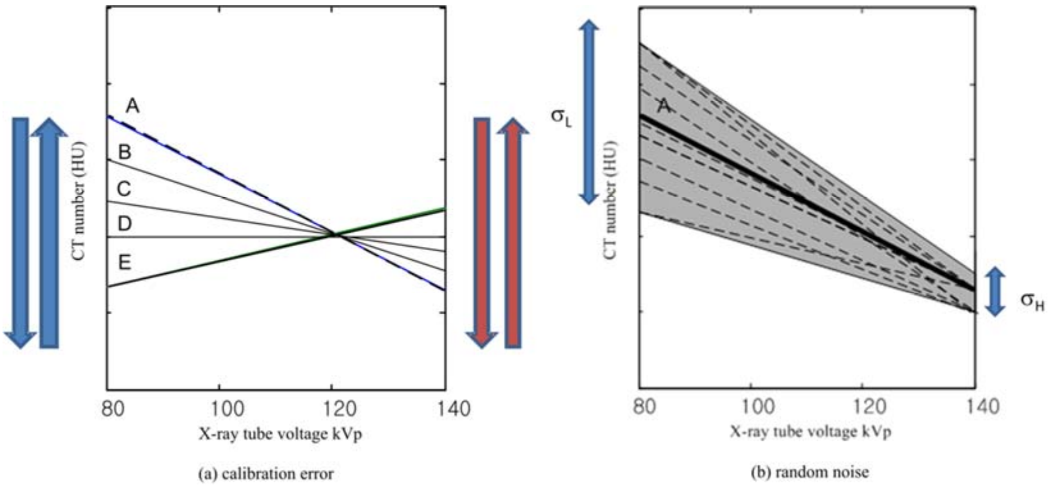

(a) calibration error

(b) random noise

Figure 12. Calibration error and random noise. (a) The calibration error of either 80kVp or 140kVp compromises the measurements of attenuation by biasing CT values indicated by arrows. (b) The randome noise distributes over the true attenuation A. In DECT, noise is smaller at high energy than at low energy.

The noise which distributes over true attenuation randomly but does not change the true attenuation direction like Figure 10b is called the random noise in this work. Most of DECT noise suppressing techniques targets to reduce this random noise without smearing the edge details.

The well-known artifact such as beam hardening and partial volume artifacts can also cause the spectral errors of DECT, but it is difficult to model them and to analyze their effect on DECT imaging. It can be said that all the above error sources together cause the spectral error which results severe noise or artifacts in DECT processing. Next, one technique is proposed to correct the spectral errors.

3.3 Dual-Energy CT Image Enhancement

Various approaches for DECT image enhancement is possible with the suggested model of Eq. (34). One simple approach may be to apply filters selectively to only the pixels of spectral error. Park et al reported that a simple linear selective filtering on the pixels of spectral error improved SNR and CNR of liver lesions without much smearing of image details [64]. In this work, a new technique for DECT image enhancement is proposed, which consists of three steps: water-reference offset correction, spectral-error correction, and adaptive anti-correlated noise reduction.

The first part of the proposed technique is to correct the water-reference offset. The CT values of water-reference must maintain at near 0 HU over X-ray energy change. The virtual 120kVp is used for the reference point because it is the most reliable in CT value estimation. First, the CT value of water is expected to be close to 0 HU on the virtual 120kVp, even though 80kVp or 140kVp image is biased. Second, the water attenuation must be unchanged over X-ray energy change. The criteria can be set up mathematically as $P_0^{'} =| 0.3P_1^{'} + 0.7P_2^{'} |< tol$ and $\Delta P^{'} =| 0.3P_L^{'} - 0.7P_H^{'} |< dtol$, where $P_L^{'}$ and $P_H^{'}$ are the low-pass filtered P_L and P_H, and tol and $dtol$ are tolerances. $P_0^{'}$ is the offset at the virtual 120kVp and

The proposed algorithm for offset correction is summarized as

- Get $P_L^{'}$ and $P_H^{'}$ after low pass filtering P_L and P_H
- $P_0^{'} = \left| 0.3P_1^{'} + 0.7P_2^{'} \right|$ and $\Delta P^{'} = \left| 0.3P_L^{'} - 0.7P_H^{'} \right|$
- Get the average m_1 and m_2 of pixel values of P_L and P_H only if they satisfy $dP^{'} < dtol \bigcap dP^{'} < dtol$
- $m_0 = 0.3m_1 + 0.7m_2$
- $P_L = P_L - m_1 - m_0$ and $P_H = P_H - m_2 - m_0$

, where tol and $dtol$ are the tolerances. Note, m_0 is the offset of water reference at the virtual 120kVp, and m_1 and m_2 are the deviations of P_L and P_H from m_0

The second part of the proposed technique is to correct the spectral errors of two low and high images. In words, if they do not satisfy the expected model of Eq. (34), the CT values of 80kVp and 140kVp images are swapped and then replaced with their virtual 120kVp values as

$$\begin{aligned} P_L^{'} &= 0.3P_L + 0.7P_H \\ P_H^{'} &= 0.7P_L + 0.3P_H. \end{aligned} \tag{36}$$

Such weighting factors came from the fact that the virtual 120kVp are the best in SNR [18], which was also verified in my analysis of DECT images. This spectral averaging ensures that high density materials attenuate more and their attenuations decrease more rapidly than lower density materials as the model of Eq. (34) predicts.

It is much probable that high density materials have much higher CT values and low density materials have lower CT values at 80kVp than at 140kVp. For example, if the pixel belongs to the contrast enhanced tissue, it cannot be true that $P_L = 50$ HU at 80kVp and $P_H = 100$ HU at 140kVp because iodine has much higher attenuation at 80kVp. It is much probable that 100 HU is close to the true CT value of 80kVp image. On the other hand, if the pixel belongs to fatty tissue, it is not expected that its CT value is -50HU at 80kVp and -100HU at 140kVp. .

Whether the pixel pair satisfies DE attenuation model of Eq. (34) or not affects dramatically to the resulting density maps of material decomposition. Its effect on two-material decomposition is presented in Figure 13. The mean values of 5x5 pixels were measured for two adipose-tissue regions of one-patient DECT images. The plots (a) and (c) are CT values over x-ray tube voltages, and the plots (b) and (d) are the corresponding density map values. Note that the density maps were obtained by solving Eqs. (26) with the assumption of effective energy 53keV and 72keV for 80kVp and 140kVp images, respectively, and the

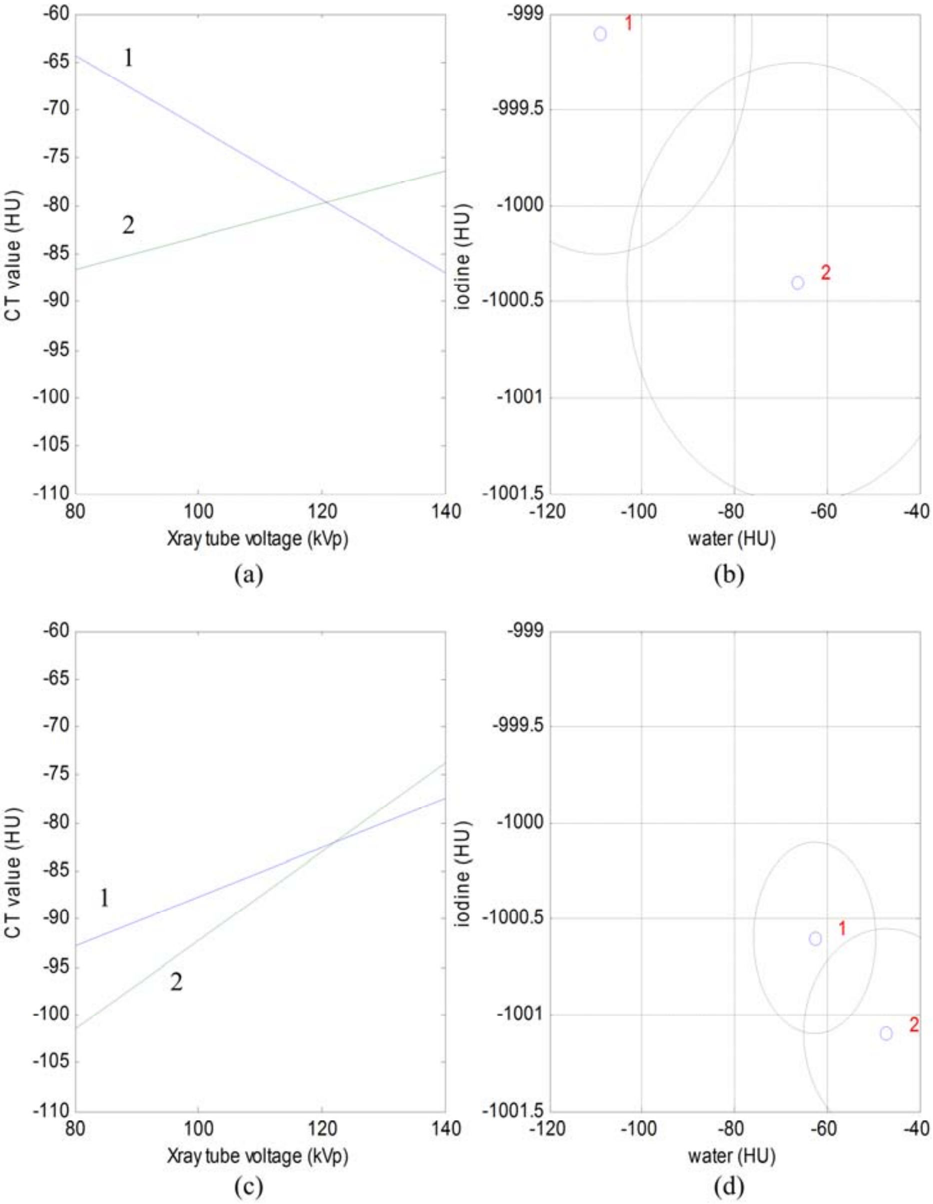

(a) (b)

(c) (d)

Figure 13. Effect of DECT spectral errors on density maps. These are the mean values of 5×5 pixels (3.13mm×3.13mm) which were measured in two adipose tissue regions, next to each other, of one-patient DECT images. The plot (a) is for the CT values over x-ray tube voltages and (b) is for density map values. They have the same mean value of -80 HU at 120kVp in plot (a), but show totally different attenuations over x-ray energy change, and their density map values are so different that they must be obviously classified as different tissues. The plot (c) and (d) are the results after replacing the pixel values by their weighted averages. Note the attenuation and density map values were also changed in (c) and (d), for they were balanced with neighboring pixel values, but the virtual 120kVp changed little (about 1HU). Note the standard deviations of density maps were represented by the radius of circle were reduced significantly by the spectral-error correction.

density-map values were converted to Hounsfield units as $P = (\rho - 1) \times 1000$ so that 0 HU is 1 mg/ cm^3 and -1000 HU is 0 mg/cm^3. In plot (a), the two regions of interest (ROI) of the original images have the very similar mean value of -80 HU at the virtual 120kVp but show totally different attenuations over x-ray tube energy change. As a result, they must be classified as different tissues by the two-material decomposition. The two-material decomposition result suggests in plot (b) that the region 1 is iodine-enhanced adipose tissue and the region 2 is adipose tissue. However, the regions are expected to be a similar adipose-tissue type because they are just next to each other, and any contrast enhancement and anatomical feature difference between two ROIs was hardly noticeable. In addition, their CT values at virtual 120kVp are that of adipose tissue.

A typical adipose tissue increases its CT values at 140kVp as the region 2 does in Figure 13a and has negative values in iodine map (P<-1000 HU, region 2 in Figure 13b). If it decreases at 140kVp due to error or noise as the region 1 does in Figure 13a, its iodine map value becomes positive (P>-1000HU, region 1 in Figure 13b). The change of the water-density value becomes more dramatic in Figure 13b, even though the two ROIs have very similar CT numbers at 120kVp. The plots (c) and (d) of Figure 13 are the results after processed by the proposed spectral-error correction algorithm. After processed by the proposed spectral-error correction, the water-density value of region 1 changed from -110 HU to -65 HU so that they can are classified the similar tissue type in Figure 13d. Note the attenuation and density map values were also changed in (c) and (d), for the mean values were changed after the spectral-correction, but the virtual 120kVp changed little (about 1HU), and the standard deviation of density maps reduced significantly. The opposite situation of soft tissue will cause severe distortion in the resulting density maps, which explains why high pixel noise is observed and problematic especially in the density maps of two-material decomposition.

In the actual implementation of the spectral-error correction of Eq. (36), several aspects have to be considered. Noise analysis on DECT images showed that zero-crossing pixel pairs ($P_L \cdot P_H < 0$) must be treated separately. Such zero-crossing pixel pairs were expected to be cancelled out or be close to 0 HU, but many pixels were too deviated and appeared like spikes. For an example in abnormal patient DE images, one pixel pair showed that $P_L = -17$ HU and $P_H = 178$ HU, and so $P_0 = 120$ HU. Its low-energy value -17 HU suggests that it belongs to fatty tissue, but its high-energy value indicates that it is the contrast-enhanced soft tissue, which is contradictory, and its virtual 120kVp value of $P_0 = 120$ HU judges it to a contrast-enhance tissue. However, Eq. (35) suggests it is an error. I found that there are many such pixel-pairs in dual-energy images that cause spike-like noise in the final images, especially in density maps. One possible solution is to apply the smoothing filter or the median filter to such pixel pairs. Median filter is the standard choice to remove such spike-like errors while preserving edge details [67].

Another important consideration is that the model of Eq. (34) cannot be generalized. Fatty liver tissue increases CT value at 140kVp up to 15 HU depending on the contribution of fatty component [33]. In addition, ten Hounsfield-unit difference is hardly discernible in CT imaging due to the system noise and limitation. The CT accreditation program of American College of Radiology (ACR) requires that the water reference value be within ± 7 HU for abdominal imaging [65]. Therefore, correcting such errors of Eq. (35) by replacing them with weighted averages should be performed only if the difference of pixel pair exceeds certain tolerance.

The third step of the proposed method is to suppress the random noise using the correlated noise reduction method. It has been originally proposed by Kalender et al. [62]. Kalender's correlated noise reduction (CNR) is based on the finding that the noises of two density maps m_1 and m_2 in Eq. (26) are negatively correlated and can be balanced on the reference attenuation. In CNR, the new density maps $m_1^{'}$ and $m_2^{'}$ after filtering have to satisfy the constraint to preserve the local mean values of $\bar{m}_1$ and $\bar{m}_2$ as,

$$\left[u_1(m_1^{'}-\bar{m}_1)\right]^2+\left[u_2(m_2^{'}-\bar{m}_2)\right]^2=\min. \qquad (37)$$

Its effectiveness on noise suppression without much loss of image detail has been proved [61]. However, I found that the CNR does not correct the spectral error of Eq. (35), even though it suppresses random noise effectively and preserves the local mean values. By combining the proposed offset correction and spectral-error correction, CNR can improve its performance. In words, it is the main idea of the proposed technique to make spectral errors distributed like random noise over true attenuation, mixed and balanced with neighborhood pixel values by CNR.

In this work, the adaptive correlated noise reduction with the gradient constraint (algorithm A2b in the paper [62]) is used because it appears to preserve details of real patient images better than any other algorithms suggested in their paper. From now on, the adaptive correlated noise reduction with a gradient constraint is denoted as KCNR.

In the KCNR algorithm, differentiating the constraint of Eq. (37) leads the new density map values which minimize the constraint as

$$\begin{aligned}\bar{m}_1 &= m_1-\left(1-\varepsilon^2\right)C/u_1\\ \bar{m}_2 &= m_2-\left(1-\varepsilon^2\right)C/u_2,\end{aligned} \qquad (38)$$

where the correction term C and the control parameter ε are defined with a gradient threshold ε_g as

$$C=\left[u_1\Delta m_1-u_2\Delta m_2\right]/2, \qquad (39)$$

$$\varepsilon = \min \begin{cases} \left|\nabla P_0\right| / \varepsilon_g \\ 1 \end{cases} \tag{40}$$

These correction terms are obtained from the constraint of Eq. (37), and more detailed formulation should be referred to the original paper [62]. In summary, the proposed algorithm is as

- Offset correction
- New $P_L^{'}$ and $P_H^{'}$ after median filtering if $P_L \cdot P_H < 0$
- New $P_0^{'} = 0.3P_L^{'} + 0.7P_H^{'}$
- Replacing pixel $P_L^{'}$ and $P_H^{'}$ with p_L and p_H ,

  $$\begin{aligned} p_L &= 0.3P_L + 0.7P_H \\ p_H &= 0.7P_L + 0.3P_H , \end{aligned} \quad \text{only if } P_0^{'} \cdot \left(P_L^{'} - P_H^{'}\right) < 0 \cap \left|P_L^{'} - P_H^{'}\right| > dtol$$

- Median filtering if $P_0^{'} \cdot \left(P_L^{'} - P_H^{'}\right) < 0,$
- KCNR (adaptive correlated noise reduction with a gradient constraint)

, where tol and $dtol$ are tolerances. The final median filtering prevents spreading of any high peak noises to the resulting images. Finally, the KCNR balanced the spectral-error corrected pixels with neighboring pixel values, of which effect is discussed later.

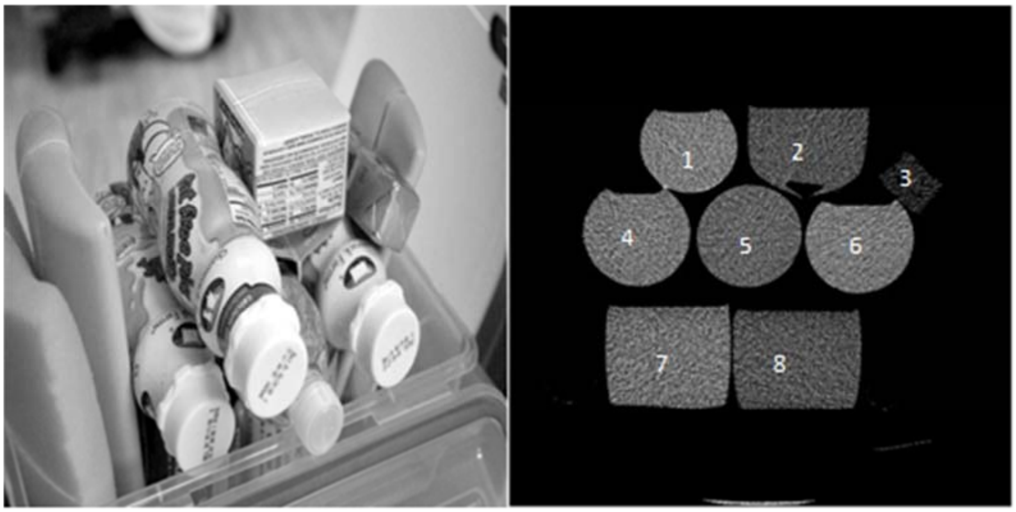

Figure 14. Milk phantom (see Table 1 for the type of materials)

	Material	Density (g/m^3)	Fat (g/ m^3)	Ca (g/m^3)
1	Fat free milk (calcium enhance)	1.033	0.000	0.0025
2	Whipped cream	0.981	0.330	0.0013
3	Butter	0.913	0.714	N/A
4	Regular milk	1.024	0.037	0.0013
5	Water	1.000	0.000	0.0000
6	2% milk	1.030	0.020	0.0013
7	Half & Half	1.021	0.117	0.0013
8	Heavy whipping	0.985	0.400	0.0013

Table 1: Milk phantom descriptions. The density and the amount of fat and calcium were calculated from the product nutrition information on labels.

3.4 Phantom and Patient Studies

In order to verify the model of Eq. (34) and the proposed technique, phantom studies were performed with milk products of different fat and calcium contents and whole chicken meat using a dual-energy software package of a 64-detector CT system (LightSpeed VCT, GE Healthcare). In the dual-energy mode of this system, two consecutive scans of 80kVp and

140kVp imaging are performed for a single acquisition in total 1.8-seconds including two 0.8-second gantry rotations and 0.2 seconds for switching tube settings.

First, eight different materials of milk, water and butter were prepared as shown in Figure 14. DECT imaging was performed with a modified adult abdomen protocol (helical, medium body filter, and 0.625mm slice thickness, 600mA for 80kVp and 342 mA for 140kVp). The images were reconstructed by filtered backprojection using the standard kernel and 32cm diameter field of view. CT values and density map values of materials were measured over 20×20 pixels (1.25cm×1.25cm), and they were compared before and after processed by the proposed technique. KCNR-only processed ones were also compared.

In addition, dual-energy imaging of whole chicken meat were also acquired (medium filter, 28cm field of view, 0.625mm slice thickness, 600mA for 80kVp and 342mA for 140kVp, standard kernel). The purpose of this chicken meat phantom imaging was to verify the model of Eq. (34) and offset correction algorithm for the real tissue imaging without water reference.

This technique was also applied to HIPAA (Health Insurance Portability and Accountability Act)-compliant patient abdomen DE images. The patient scans were performed in contrast-enhanced CT (CECT) imaging, and the CECT protocol was 338mAs for 80kVp and 193mAs for 140kVp scans, 0.675m slice thickness, and large body filter and liver portal venous phase (70s-delay scan after the initiation of contrast agent).

All the scans were performed after daily automatic system calibrations at Mayo Clinic, Scottsdale, AZ, in order to minimize calibration error. The post-processing was coded and performed using Matlab (Mathworks Inc., MA, USA). The tabulated data of mass attenuation coefficients of water and iodine were obtained through NIST, USA, and their

No	Material	Density (HU)	Original (HU)			Proposed Method (HU)		
			80kVp	140kVp	P_0	80kVp	140kVp	P_0
1	Fat free milk	33	39.5±8.1	39.5±6.3	39.6±5.3	51.2±5.9	44.1±4.1	45.8±4.6
2	Whipped cream	-19	-21.4±10.0	-8.3±6.3	-11.4±5.6	-14.1±5.2	-4.0±3.6	-6.3±5.6
3	Butter	-87	-137.5±18.2	-109±16.8	-116.0±16.6	-130.1±18.6	-103.4±16.2	-109.6±16.9
4	Regular milk	24	32.2±10.3	29.3±6.2	29.5±5.6	42.1±2.8	34.8±4.8	36.5±5.3
5	Water	0	-10.3±16.8	-7.9±9.8	-8.6±9.1	-2.8±11.2	-2.5±6.4	-2.6±7.4
6	2% milk	30	34.1±11.7	31.9±7.0	32.4±6.2	44.6±44.6	35.3±5.6	37.4±6.0
7	Half & Half	21	22.5±13.4	24.3±8.7	23.9±7.8	35.5±8.6	28.2±6.0	29.9±6.5
8	Heavy whipping	-15	-18.3±12.3	-7.0±7.9	-9.6±7.2	-9.8±6.2	-4.4±2.2	-3.9±4.7

Table 2: CT values of the milk phantom. All the values were measured on 20x20 pixels (1.25cm × 1.25cm). The CT values of the propose method are offset-corrected and are similar to the values of original image except the offset correction. The water reference values of the original images are biased -10.3 HU at 80kVp and -7.9 HU at 140HU and the both P_0 values are within 1% accuracy to the expected density values of the materials except the butter, which has air spaces inside and so shows relatively a large deviation. And the density values were converted to Hounsfield units by $(\rho-1)\times1000$.

No	Material	Density (HU)	Original (HU)			Proposed Method (HU)		
			Water	Iodine	Density	Water	Iodine	Density
1	Fat free milk	33	39±14.8	-1000.0±0.4	38.6±14.1	37.3±4.3	-999.7±0.1	38.7±4.0
2	Whipped cream	-19	4.8±15.6	-1000.6±0.5	4.3±13.3	5.7±3.1	-1000.4±0.1	3.7±3.5
3	Butter	-87	-79.6±21.0	-1001.2±0.4	-76.3±19.7	-77.8±16.6	-1001.1±0.3	-83.1±16.9
4	Regular milk	24	22.8±14.7	-1000.0±0.5	28.3±14.3	27.8±3.6	-999.7±0.1	29.2±4.4
5	Water	0	-4.1±22.7	-1000.1±0.7	-4.6±19.8	-2.1±4.9	-1000.0±0.2	-2.2±5.7
6	2% milk	30	28.0±18.5	-999.9±0.6	28.8±17.5	26.2±5.3	-999.6±0.2	28.1±6.0
7	Half & Half	21	25.6±19.4	-1000.1±0.6	28.9±21.2	21.3±4.5	-999.7±0.2	22.7±5.5
8	Heavy whipping	-15	4.7±17.5	-1000.5±0.5	5.9±18.5	5.4±4.0	-1000.3±0.1	3.9±4.6

Table 3: Material decomposition of the milk phantom. All the values were measured on 20x20 pixels (1.25cm × 1.25cm). The accuracy of the original and the proposed are within 0.3% except whipped cream and heavy whipping cream. They showed 2% errors. Note that the proposed method improved SNR over 300~500% in both water and iodine maps except the butter, which has air spaces inside, and produced high quality density map. It made better material differentiation (see Figure 13).

mass attenuation functions $u(E)$ were estimated using polynomial regression above k-edge absorption lines.

Assumed 53keV and 72keV effective X-ray energy for 80kVp and 140kVp images respectively, two-material decomposition was performed using Eq. (26) for water and iodine basis materials. For the correlation noise reduction (KCNR), a 5×5 pixel mask and the gradient threshold $\varepsilon_g = 10$ were used. SNR and CNR between two regions of interest a and b were defined as

$$\begin{aligned} SNR &= \left[mean(P) + 1000 \right] / std(P) \\ CNR &= \left[mean(P_a) - mean(P_b) \right] / std(P_a), \end{aligned} \tag{41}$$

respectively. Note that the CT value of air 1000 HU was used as the signal reference in Eq. (41).

3.5 Results

The measurements of CT values and density maps were presented in Table 2 and Table 3, respectively. Note that the density values were represented in Hounsfield units by using the relation, $(\rho - 1) \times 1000$, and so 1 HU is 1mg/cm^3. In the original images, the high density milk materials showed little decrease or few changes in their CT numbers at 140kVp, but the low density milk materials of heavy fat content increased their CT number about 10HU as expected (see Table 2). The attenuations of the half-and-half milk and the calcium-enhanced fat-free milk were somewhat contrary to what was expected. The half-and-half milk increased about 2HU at 140kVp, and the calcium-enhanced fat-free milk did not change its CT values. However, the water reference shows offset errors (-10.3 HU at 80kVp and -7.9 HU at 140kV), even though the automatic system calibration was performed before the scan. So, the offset correction was applied to the original images using the proposed offset-correction algorithm, which produced -2.8 HU offset at 80kVp and -2.5 HU offset at 140kVp for the water reference (Figure 15b). Note that Figure 14b is the result that only offset-correction technique was applied without the spectral-error correction to the original images. The result images still have small offset errors (<3HU) but it is reasonable value for water reference. Most of all, the water offset values became well balanced at both 80kVp and

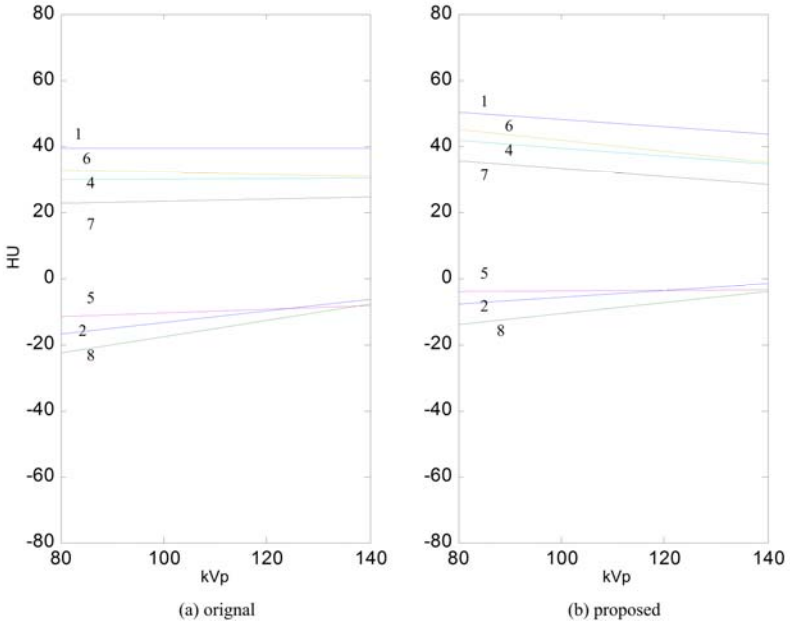

Figure 15. Offset correction for the milk phantom. In the original image (a), the CT value of water (number 5) is biased about -10HU at 80kVp and -8.3HU at 140kVp, which was corrected to -2.8 HU at -80kVp and -2.5 HU at 140kVp by the proposed offset-correction method (b). Note that the attenuation changes of other materials after the correction, which allows the better differentiation in two-material decomposition. Note the materials are labeled by the numbers, and see Table 1 for their detailed descriptions.

140kVp after the offset correction so that all the materials followed the expected attenuation trends in Figure 15b - heavy density material deceases and low density material increases CT number at 140kVp. For the water reference, the proposed method improved SNR by 46% and by 53% for 80kVp image and 140kVp image respectively, and the virtual 120kVp also showed 30% SNR improvement. Although not so impressive, it should be considered that this phantom was small and well-exposed so that the original images itself are of high quality. On the other hand, the proposed method improved the resulting density maps dramatically of 300~500% noise suppression, except for the butter. Butter has air space inside and so it is not homogenous.

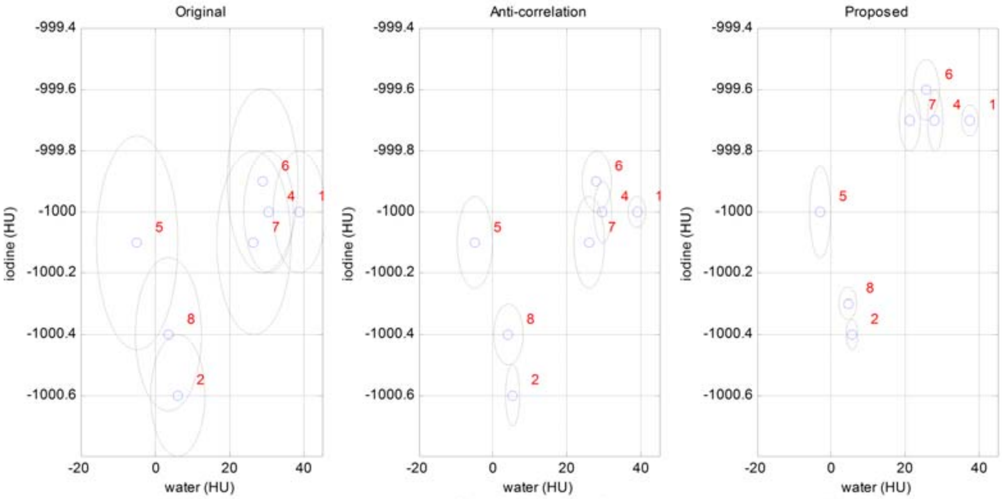

(a) orignal (b) anti-correlation only (c) proposed

Figure 16. Material differentiation of the milk phantom using two-material decomposition. See Table 1 for the material description. All the values were measured on 20x20 pixels (1.25cm × 1.25cm), and the dotted circles are the area within the standard deviations. In the original density maps (a), the materials are heavily overlapped and hardly differentiable due to the noise, and KCNR-only (b) suppressed noise effectively. The propose method (c) are superior in both correcting bias and material differentiation. Note that water (number five) is expected to be positioned at 0 HU (1g/cm^3) on the water density map and -1000HU (0g/cm^3) on the iodine map, but water is biased in the original maps while it is corrected by the proposed method (c). The anti-correlation-only technique failed to correct the bias. The butter is not included in these plots because of its obvious separation.

In order to verify its effectiveness on material differentiation, I compared the resulting density maps of the proposed technique with the original density maps and the KCNR-only ones and presented the results as the plots of iodine-density value versus water-density values in Figure 16, where the dotted circles are the standard deviations and materials are labeled with numbers (see Table 1 for the material description). The comparison clearly shows that the density maps of proposed technique improved material differentiation over the original and the KCNR-only. In the original density maps (Figure 16a), the materials are heavily overlapped and hardly differentiable due to the

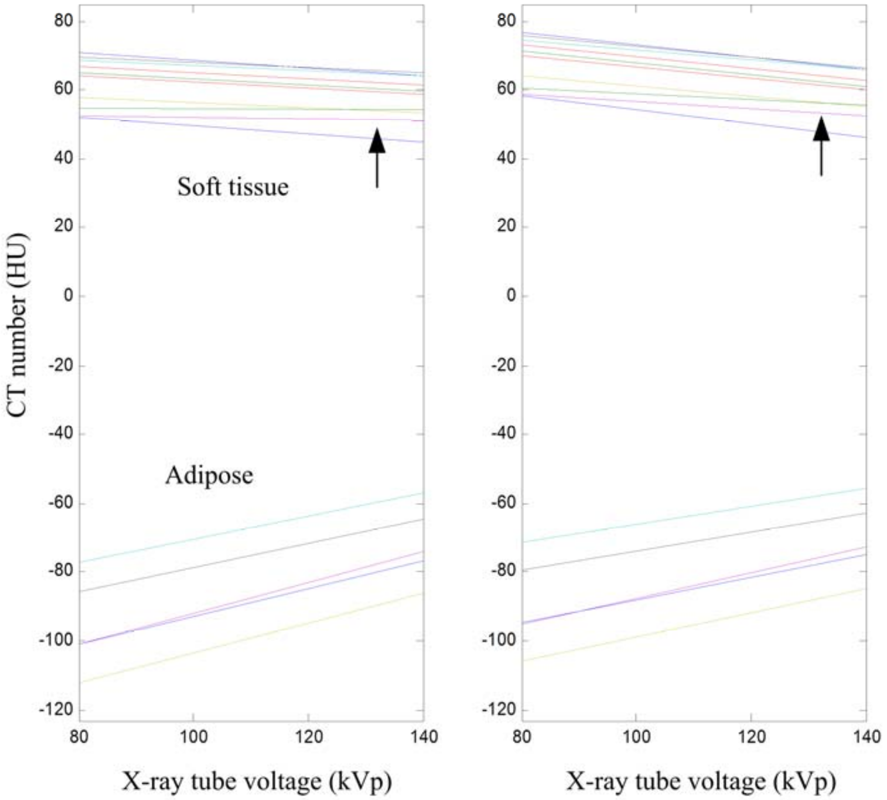

(a) Orignal

(b) Offset-corrected

Figure 17. Offset correction for the chicken meat phantom. The original images (a) were biased by -4.6 HU at 80kVp and -0.03 HU at 140kVp. Although 140kVp was not biased, the bias of 80kVp affects the measurements of energy dependency of x-ray attenuation of the materials. After correcting the bias by the proposed technique, the tissue in arrow showed the typical attenuation trends of soft tissue as a result.

noise, and the KCNR-only (Figure 16b) suppressed noise effectively but failed to correct the offset and spectral errors.

The water reference (material five in Figure 16) is expected to be positioned at 0 HU (1g/cm^3) on the water density map and -1000 HU (0g/cm^3) on the iodine map, but water was biased in the original map and the KCNR-only map, while the proposed method corrected the bias error. In addition, the standard deviation of water was 10.0 HU for KCNR-only while 6.3 HU for the proposed method. The proposed method improved KCNR by correcting bias and spectral error and resulted in better material differentiation

(Figure 16c). Note that regular milk, 2% milk and half-and-half milk, which are labeled 4, 6, and 7 respectively in Figure 16, have very similar density and small differences of fatty content so that they are overlapped severely even by KCNR, but the proposed technique differentiated them in a better way (Figure 16c). The butter is not included in these plots because it is easily differentiable due to its low density.

The milk phantom included water reference, but such reference is not available in routine clinical CT imaging. The imaging of whole chicken meat was performed in order to check how the attenuation changes in real tissue and how the bias affects to real tissue. The original DECT images of the chicken phantom were biased -4.6 HU at 80kVp and -0.03 HU at 140kVp (Figure 17a). These bias values were detected by the proposed technique. Although 140kVp was not biased, the bias of 80kVp affected the measurements of energy dependency of X-ray attenuation of the materials. It resulted in the attenuation change of the tissue in arrow and was corrected by the proposed technique and shows the typical attenuation trends of soft tissue after the correction (Figure 17b).

The proposed techniques are applied to the real patient abdominal images (Figure 18). For the noise reduction for these patient images, the gradient threshold $\varepsilon_g = 10$ HU was used. It is very conservative approach to preserve the detail. Only the gradient difference of less than 10 HU trigger noise reduction [see Eq. (40)]. The proposed technique suppressed noise of the original images without any noticeable loss of detail and improved the contrast between liver lesion (number 1) and contrast-enhanced liver parenchyma (number 2). For the 80kVp image, the proposed method improved SNR and CNR over the original by 165% and 150%, respectively, but it showed similar SNR and CNR performance to those of KCNR-only. For

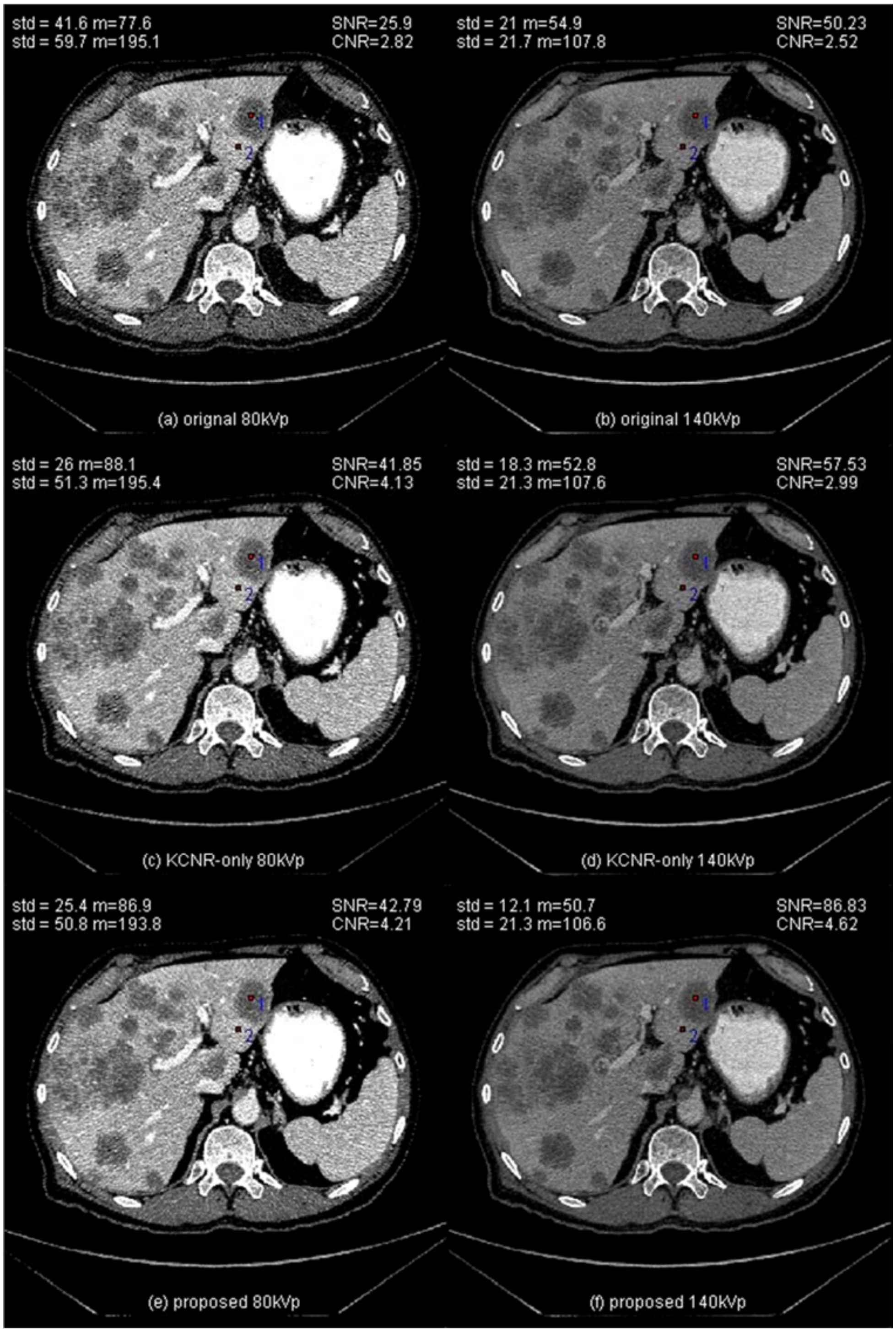

Figure 18. Abdominal image results. The proposed improved both 80kVp and 140kVp images without smearing edges, compared to the original and the KCR-only images. Note SNR of live metastasis lesions and CNR between lesion and enhanced live parenchyma. (WW=400, WL=130 for all the images).

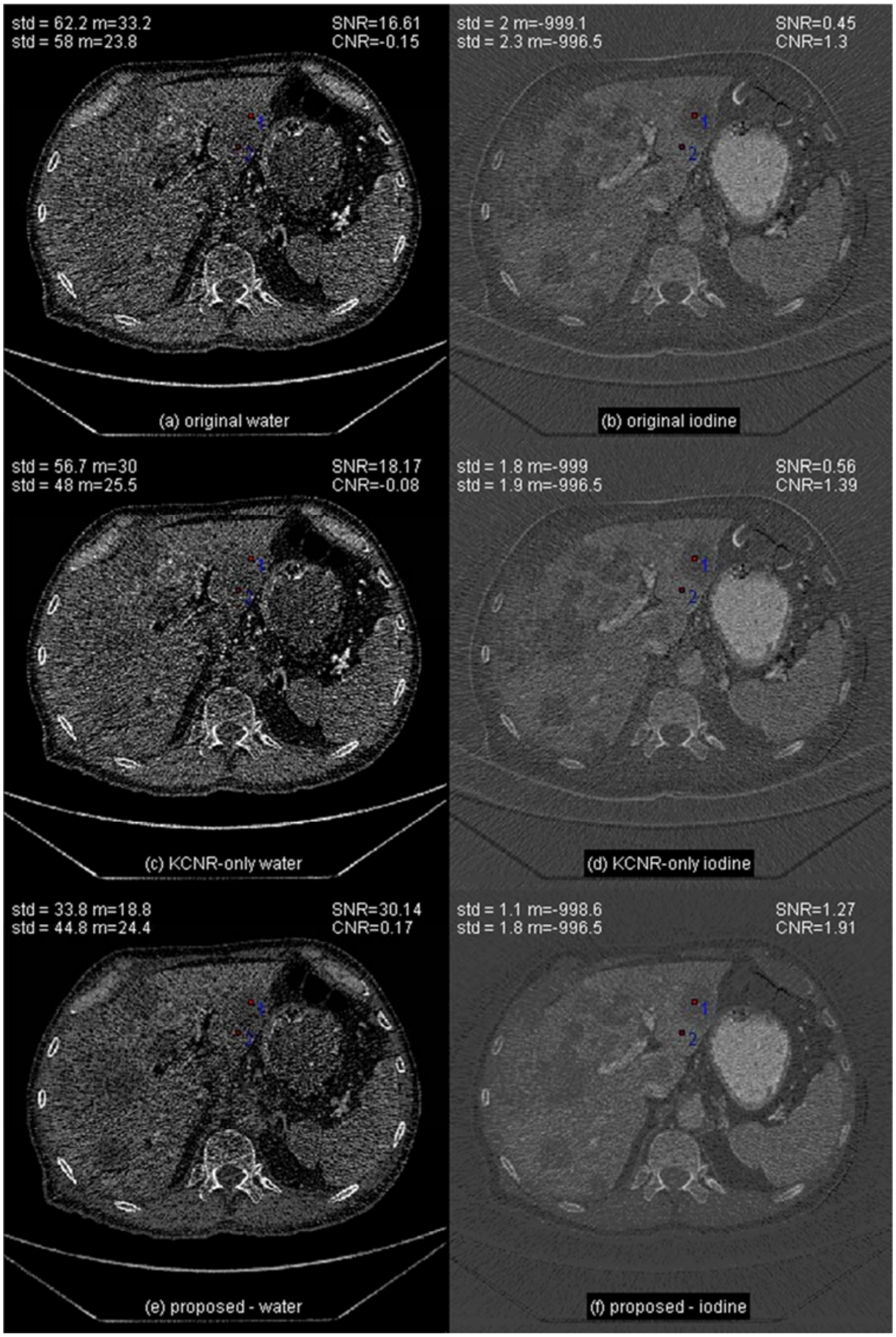

Figure 19. Material decomposition of abdominal images. The hypodense liver metastases are noticeably visible in the water density map of the proposed method, but those of the original and the KCNR-only density maps are hardly differentiable.

the 140kVp image, the proposed method improved SNR and CNR by 174% and 183% over the original and 150% and 155% over KCNR-only. The improvement on density maps was more noticeable.

Such small differences between the images of KCNR-only and the proposed method made a big difference in the resulting density map values. The SNR improvements on the water density map (Figure 19e) were 181% over the original (Figure 19a) and 160% over KCNR-only (Figure 19c) and in the iodine density map 280% over the original and 227% over KCNR-only. CNR is also improved. The proposed method improved SNR and CNR for both images and density maps. However, there were noticeable changes of 10 HU at 80kVp especially in liver metastases lesions for either KCNR-only or the proposed method. The average mean values of KCNR-only and the proposed method had 2 HU differences in both 80kVp and 140kVp images and the difference between CT values of 80kVp and 140kVp were maintained as 36HU. For the KCNR-only, the water-density map value was 30±56.7 HU and the 18.8±33.8 HU and -998.6±1.1 HU, respectively.

CHAPTER 4

DISCUSSION

4.1 Comparison to Correlated Noise Reduction

The proposed method improved SNR, CNR and material differentiation. The improvement was mainly attributed to the spectral-error correction. Its effect is dramatic in that the spectral-error correction algorithm alone without KCNR made 170% SNR improvement for water density maps and 300% for iodine density maps over the original density maps for the abdominal images. The KCNR did not contribute much to the SNR improvement of ROI due to the low threshold of the gradient constraint applied. In this work, the threshold of the gradient constraint $\varepsilon_g = 10$ was used for KCNR. Only less than 10 HU difference triggered adaptive noise reduction and the amount of noise reduction was controlled further by the amount of gradient to the neighborhood pixel values [see Eqs. (38)~(40)]. The high threshold of gradient constraint improves SNR but causes the degradation of edge details. Originally, the non-adaptive KCNR was tried but smearing edge detail was too noticeable. When compared with all the KCNR methods proposed by Kalender et al.[62], the adaptive KCNR with the gradient constraint of a reasonable threshold was the most effective in preserving the edge details as well as in suppressing the noise, but it was my subject evaluation.

It appeared that the original KCNR suppresses only the random noise with respect to the reference attenuation and failed to correct the spectral error. The proposed method corrects the spectral errors by replacing them with the weighted average values of low and high energy images. For example, all the pixel pairs of Figure 3 have the same CT value at 120kVp. Without any priori information, it is impossible to judge which one is the true

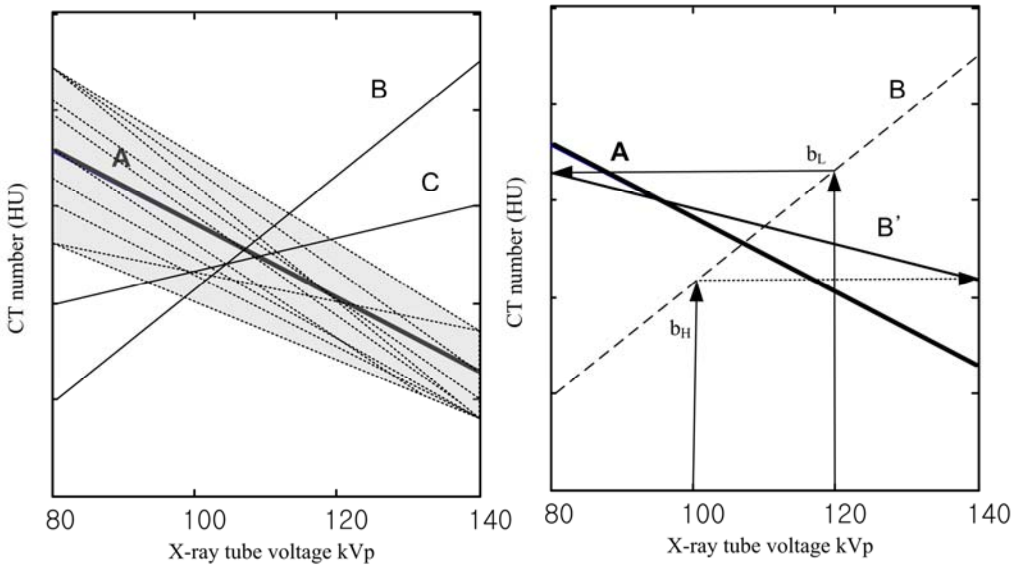

Figure 20. Spectral errors and random noise. For a typical contrast-enhanced tissue, the random noise distributes like the dotted lines within a certain range (gray regions) over the true attenuation of A, but the spectral errors are far deviated and in the opposite direction like B and C in the left plot. The proposed algorithm for the spectral-error correction replaces P_L and P_H of the attenuation B with b_L and b_H, which are the weighted sum of 80kVp and 140kVp, respectively so that B becomes B' like random noise over A in the left plot. Finally, the random noise is balanced with neighbor pixel values by KCNR.

attenuation or error. The proposed model of Eq. (34) or (35) provides such a priori-knowledge on tissue attenuation that E is an error for the contrast-enhance soft tissue, but C and D are more likely unenhanced tissues. Therefore, uncertainty is reduced, and so image quality and material differentiation can be improved.

4.2 Spectral Error Correction

The proposed algorithm is schematically explained for a contrast-enhance tissue in Figure 20. The random noise over a true attenuation A of a contrast-enhance tissue will be like the dotted lines and distributes over A within a certain deviation as the gray region in the left plot. It is the spectral error that is too far deviated and in the opposite direction from the true attenuation A as the attenuations of B and C do. The spectral error of B does not satisfy the condition of Eq. (34), so that the proposed algorithm replaces P_L and P_H of the attenuation B with b_L and b_H, which are the weighted sum of 80kVp and 140kVp as

$$\begin{aligned} b_L &= 0.3P_L + 0.7P_H \\ b_H &= 0.7P_L + 0.3P_H, \end{aligned} \tag{42}$$

respectively in a way that the attenuation at 80kVp is higher than at 140kVp.

So, B becomes B' like random noise over A. Finally, the random noise is mixed and becomes balanced with neighboring pixel values by KCNR at the third step of the proposed algorithm. It is the main idea of the proposed method to make the spectral errors distributed like random noise over the true attenuation, mixed, and balanced with the neighborhood pixels values.

4.3 The Effect of Spectral-Error Correction.

The effect of the proposed spectral-error correction is demonstrated in Figure 21. The mean values of two adipose tissue regions, adjacent to each other, were measured over 5×5 pixels after one-patient DECT images were processed by KCNR-only and the proposed spectral-error correction. The plots (a-c) are for the CT values over X-ray tube voltage change and (d-f) are their corresponding density map values. In the original images (Figure 21a), the tissues have the same mean value of -80 HU at the virtual 120kVp but show totally different attenuation over X-ray energy change. Apparently, tissue 2 is an adipose tissue, but tissue 1 is less likely adipose tissue due to its attenuation trend. For both ROIs, KCNR-only decreased CT values about 10 HU at 80kVp and increased about 5 HU at 140kVp, which implies most of CT values of the ROIs are lower at 80kVp and higher at 140kVp than the CT values of the original images, but the spectral trend is still unrealistic for adipose tissue. In the density maps, KCNR-only just reduced the deviation little by balancing 80kVp and 140kVp values on the virtual 120kVp values (Figure 21b) and classified them as different types (Figure 21e).

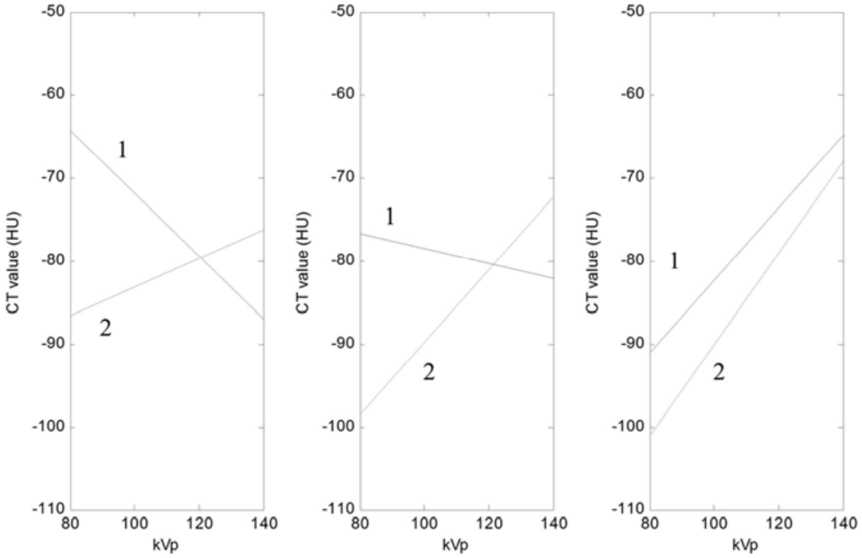

(a) original (b) KCNR-only (c) proposed

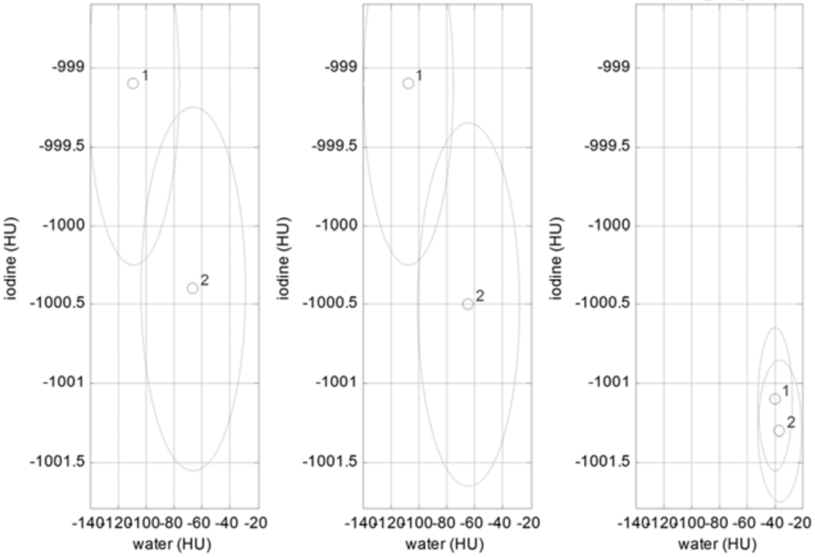

(d) original (e) KCNR-only (f) proposed

Figure 21. Spectral-error correction. These are the mean values of two adipose tissue regions (5x5 pixels) adjacent to each other in one patient DECT images. The plots (a-c) are for the CT values over x-ray tube voltages and (d-f) are their corresponding density map values. In the original images (a), the tissues have the same mean value of -80 HU at the virtual 120kVp but show totally different attenuation over x-ray energy change. (b) KCNR-only just reduced the deviation by balancing 80kVp and 140kVp values on the virtual 120kVp values. The tissue 1 does not satisfy Eq. (c) The proposed method corrected the spectral error of tissue 1 and characterized them as a similar tissue type (f) but KCNR-only judged them as different types. Note that only spectral-error correction was applied for the result (f) but it reduced noise effectively, which was reflected in the small circles of standard deviation, compared to KCNR-only.

On the other hand, the proposed method judged the tissue 1 as adipose tissue according to its CT value at 120kVp and corrected the attenuation as a typical adipose tissue. It characterized them as a similar tissue type in the resulting density maps (Figure 21f). Note that only the spectral-error correction was applied to the original images for this result, but it reduced noise effectively even without KCNR, which was reflected in the small circles of standard deviation in Figure 21f and shows the effectiveness of the proposed model.

However, it must be arguable that the attenuation of tissue 1 in Figure 21a was changed a lot by the proposed method. The virtual 120kVp value were changed about 5 HU, so its quantitation varied. It is still unclear whether the attenuation like tissue 1 of Figure 21a is an error or the true attenuation of the tissue. It is also possible that the tissue might be contrast-enhanced adipose tissue. The contrast-enhancement of adipose tissue was not discussed in literature. One possible explanation may be the partial volume effect.

There were several differences between the resulting density maps of the original and the proposed methods. In Figure 22, the density maps were presented with the original 80kVp and 140kVp images for reference. The two original 80kVp and 140kVp images are apparently misregistered, and the original density maps (Figure 22c and d) show unexpected structures on both density maps. First, unexpected contrast-enhanced structures were shown in the original water density map (thin arrow in Figure 22c) and second, artificial structure is shown in the original iodine density map (the thick arrow Figure 22d). They are the effect of spectral errors caused by misregistration. On the other hand, the density maps of the proposed method (Figure 22e and f) do not show such ghost-like structures. Compared to the original 80kVp and 140kVp images, iodine content was separated well. Both water and iodine density maps of the proposed method carry all the anatomical and morphological structures of the original 80kVp and 140kVp without such artifacts. Therefore, the proposed method corrected misregistration in some way.

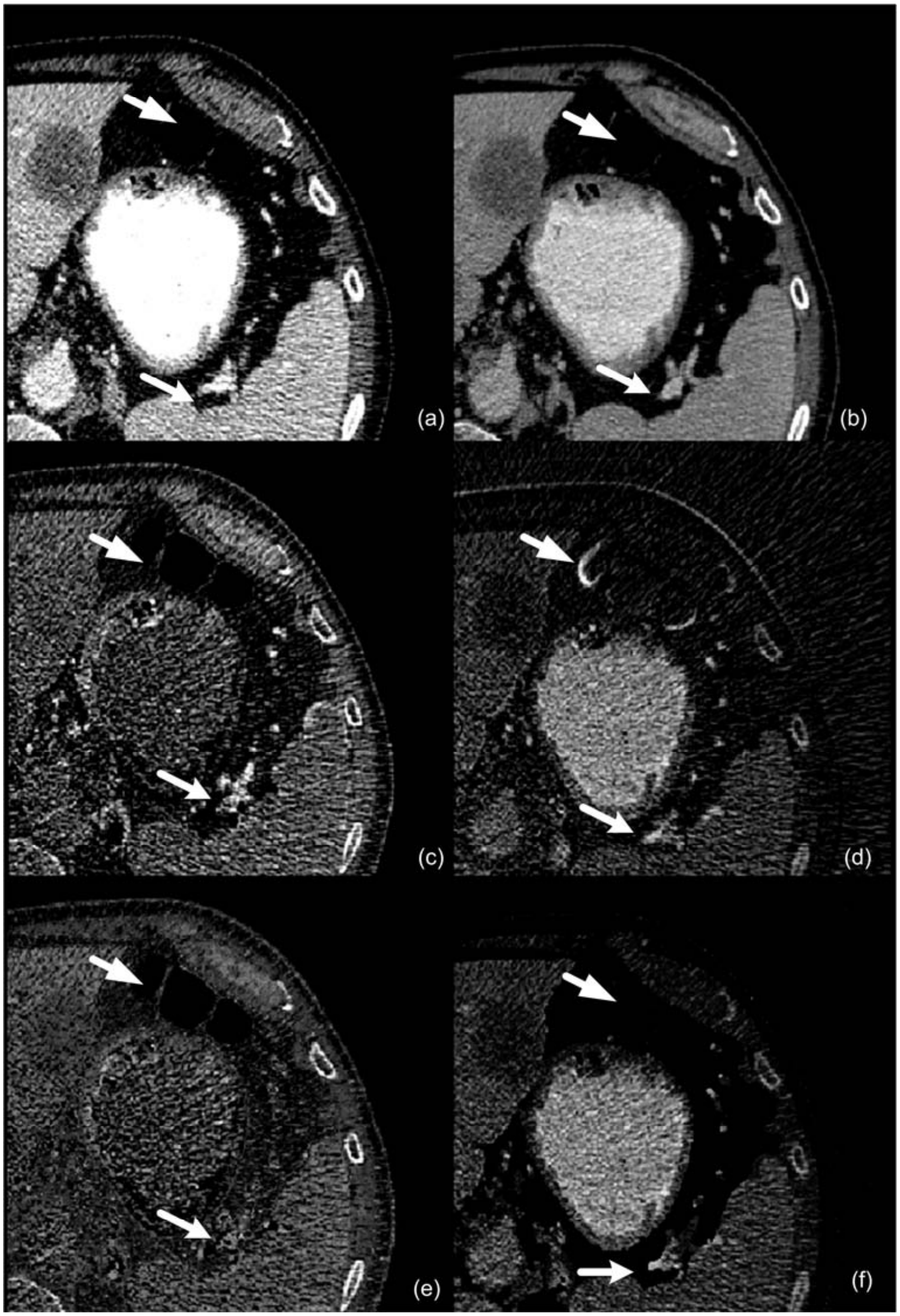

Figure 22. The density map comparison 80kVp (a) and 140kVp (c) are presented for the reference. Original water map (d) original iodine map (e) proposed water map (f) proposed iodine map. Note the misregistration of the original 80kVp and 140kVp images and the resulting differences between density map results in arrows.

For this reason, tolerances were set in the proposed algorithm. In this work, the pixel pairs were not considered as spectral errors if their difference is within 20HU even though they do not satisfy the condition of Eq. (34).

4.4 Dual-Energy CT for Material Differentiation

The primary goal of DECT is the material differentiation. In the dual-energy mode of Siemens DSCT system, the tissue signature plot is used for the three-material decomposition, in which a CT-value pair of 80kVp and 140kVp images is compared to the predefined positions of the three basis materials; fat, soft tissue, and iodine. Its relative position represents the amount of composite materials and so is used for material differentiation.

In three-material decomposition, it is assumed that the tissue consists of three materials of fat, soft tissue, and iodine. Similarly to the tissue signature plot, the density maps of two-material decomposition for the milk phantom were presented in Figure 18, in which the propose method showed the improvement in material differentiation. Here, the relation between tissue signature plot and two-material decomposition is discussed.

Tissue signature plots of the milk phantom before and after processed by the proposed were compared in Figure 24. The fatty milk products were expected to be positioned lower than the iso-line ($P_L = P_H$, solid line), but most of CT-value pairs appeared to be distributed equally over the iso-line in the original images of Figure 23a. The KCNR-only result was not so different from the original one. On the other hand, the proposed method corrected the

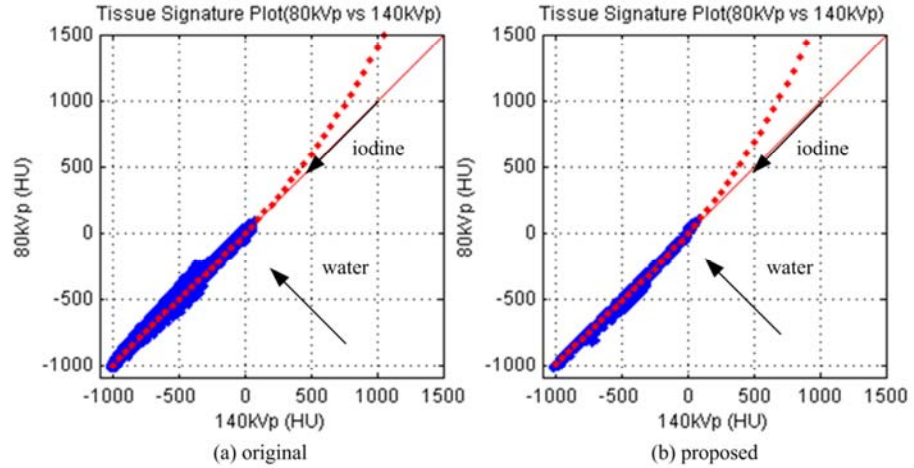

Figure 23. Tissue signature plot comparison of the milk phantom. (a) the tissue signature plot of the original images (b) the tissue signature plot after processed by the proposed method. The fatty milk products are expected to be positioned lower than the iso-line ($P_L = P_H$, solid line), but most of pixel pairs appeared randoriginal The histogram of water density map is a view to the distribution which is projected on the iso-line, and the histogram of iodine density map is a view to the distribution which is projected on the iodine attenuation line, which is about 69 degree off from the horizontal axis; $u_{L,iodine} / u_{H,iodine} = 2.35$.

spectral errors of the fatty milk in Figure 23b so that most of fatty milk is positioned in the lower part than the iso-line as the model of Eq. (34) predicted.

In Figure 24, the histograms of virtual 120kVp images and the density maps are displayed and compared before and after processed by the proposed technique. The histogram of the original virtual 120kVp image in Figure 24a already separated butter, low and high density milk products. The histogram of the virtual 120kVp image of the proposed method in Figure 24b shows the image quality improvement over the original one by high peaks with narrow widths. Moreover, the histograms of the proposed method (Figure 24d and e) clearly show the superiority of the proposed method in the material differentiation.

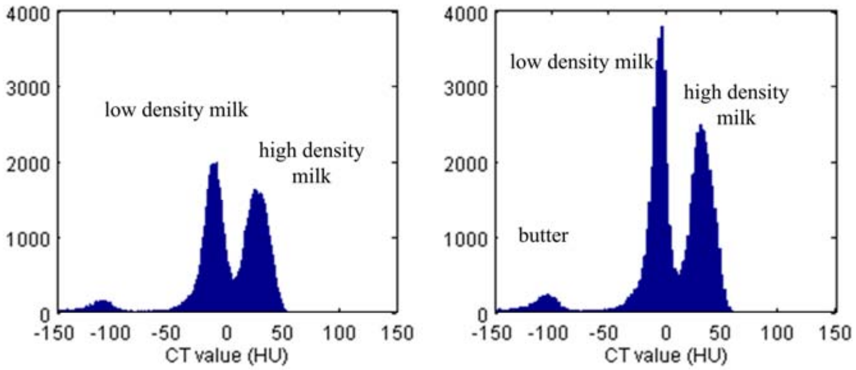

(a) original - virtual 120kVp (b) proposed - virtual 120kVp

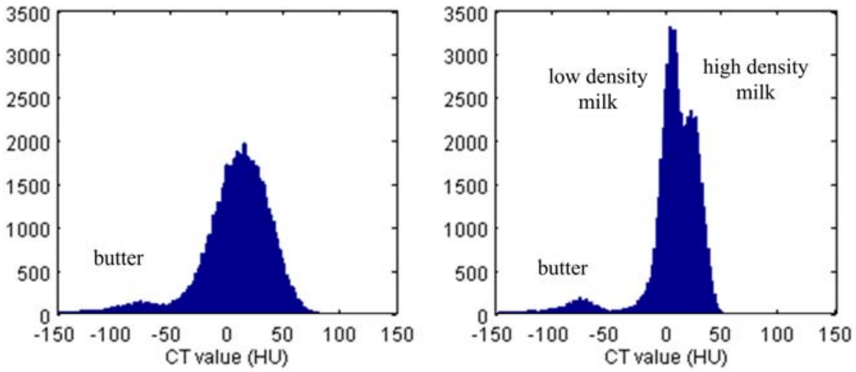

(c) original - water (d) proposed - water

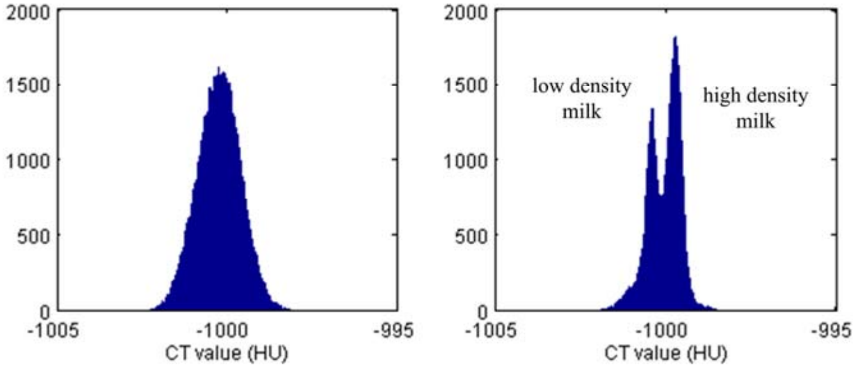

(e) original - idone (f) proposed - iodine

Figure 24. Histograms comparison of the milk phantom. (a) and (b) are the histograms of the virtual 120kVp images. (c-f) are the histograms of water and iodine density maps. The left columns are before and the right columns are after processed by the proposed method, respectively.

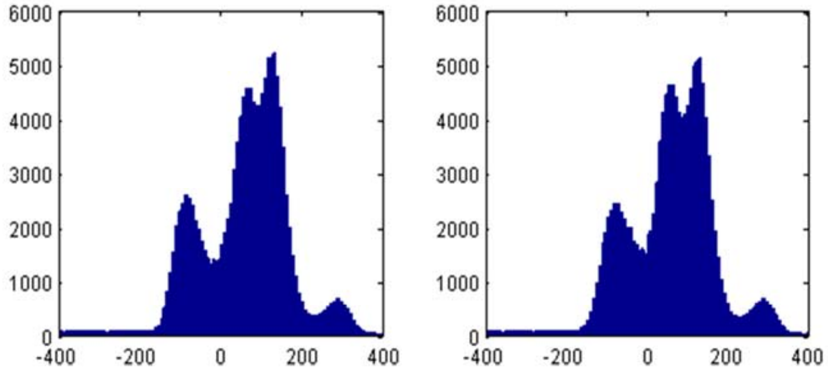

(a) original - virtual 120kVp (b) proposed - virtual 120kVp

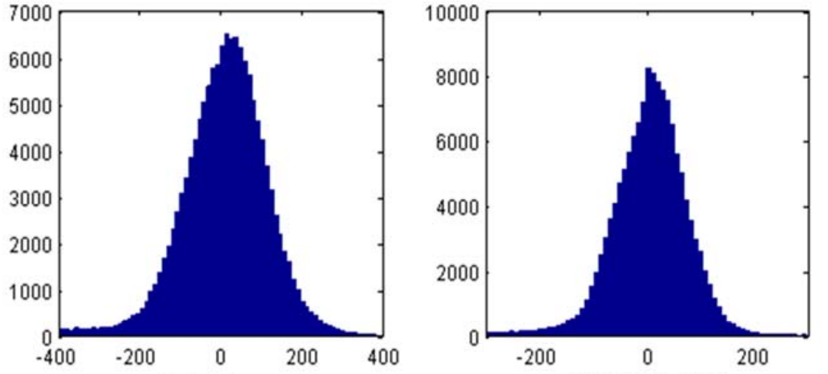

(c) original - water (d) proposed - water

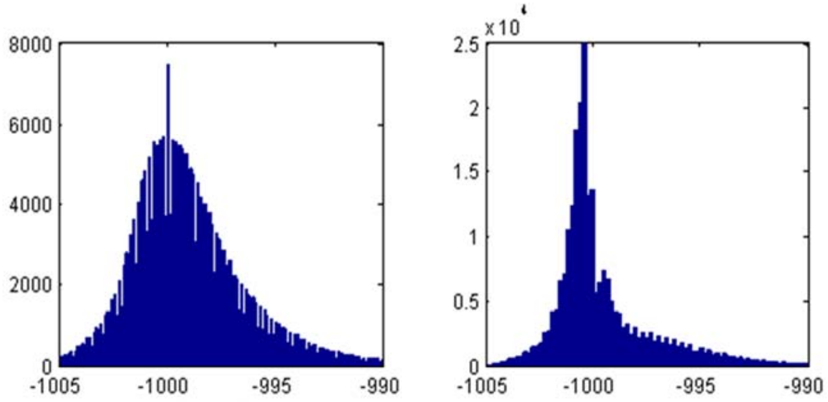

(e) original - iodine (f) proposed - iodine

Figure 25. Histogram comparison of patient images. The histogram of patient images shows the proposed method made better material differentiation, especially in the iodine map (f). Note the virtual 120kVp of the proposed method shows better distinction in soft tissue ranges. The KCNR-only result was not presented, but it did not improve separation even with higher masks and just smoothed the histogram of the original images.

Smoothing such as with KCNR may narrow the random distribution and produce better density estimation. However, such smoothing cannot recover the lost spectral information of fat and calcium.

On the other hand, the proposed method redistributed their attenuations based on the material spectral property; the attenuation of higher density material decreases relatively faster over X-ray energy changes. Most of milk contents are water, fat and calcium. Calcium attenuates faster and fat attenuates slower than water, which is reflected in the histogram of the resulting density maps of the proposed method. The proposed method can be considered as a kind of post-calibration for tissue attenuation over X-ray energy change, not for density estimation.

In addition, the histogram of patient images shows the proposed method made better material differentiation, especially in the iodine map (Figure 25f). Note the virtual 120kVp of the proposed method shows better distinction in soft tissue ranges. The KCNR-only did not improve separation even with higher masks and just smoothed the histogram of the original images, and so it was not presented.

The histogram of water density map in Figure 24 is a kind of view to the distribution of the tissue signature plot in Figure 23 from the direction orthogonal to the iso-line, on which the tissue attenuations are parallel to the water attenuation in the vector space representation of Figure 2. On the other hand, the histogram of iodine map is a kind of view to the distribution deviated from the iso-line as indicated by arrows of Figure 23. In Figure 24e and Figure 25e, the histograms of the original iodine density map shows a typical normal distribution.

4.5 Dual-Energy CT Calibration

All the analysis of DECT images leaded to a question, how DECT is calibrated. A typical calibration procedure of conventional CT imaging targets to set up a linear relationship between air (-1000HU), water (0HU) and bone (950HU), especially for major body tissue regions of -200 ~200HU. It appeared that both 80kVp and 140kVp images were calibrated for the same linear relationship for accurate density measurement and lost some spectral information. The tissue signature plot of the milk phantom (Figure 23a) shows a linear trend of attenuation in low density materials. It may show that both 80kVp and 140kVp images were calibrated for the iso-line (solid line), where the attenuation is parallel to water attenuation. The normal distribution of the iodine-map histogram may imply that they are calibrated for the same reference because the histogram shows the deviation from the iso-line.

Conventional CT imaging targets accurate density measurement so that the known density is the calibration reference. However, the main problem of CT imaging is that different material can have a similar CT value. DECT was developed in order to solve the problem. In DECT, the linear density reference should not be used for DECT calibration. It is the paradigm of single-energy CT imaging to measure density. In DECT, each low or high energy imaging should be calibrated separately at each energy level with its own reference. Fatty tissue and soft tissue attenuation references should be set differently for low and high energy.

To my knowledge, there is no standard calibration reference for DECT yet. The calibration standard for DECT should be established as soon as possible. For the conventional CT imaging, American College of Radiology (ACR) provides the CT accreditation program using the so-called ACR phantom which is used for CT system calibration and evaluation: CT value accuracy, low contrast and high contrast resolution, uniformity, and alignment test. In the

ACR phantom, there are four materials representing body tissues for CT value accuracy test: polyethylene for fatty tissues, water reference, acrylic for soft tissues, bone equivalent plastic for bone. It was observed that the CT value of acrylic increases over 20 HU at 140kVp from the value of 120HU at 80kVp (see Figure 26 and Table 5). The increasing trend is the own property of acrylic due to its high contents of hydrogen and carbon. It is very contradictory to the typical attenuation of human soft tissues. Normally, soft tissue decreases about 10HU at 140kVp. Therefore, the acrylic in ACR phantom cannot be used for the reference of soft tissue in DECT. Only in some abnormal patient cases, the CT value of fatty liver changes little or increases slightly at 140kVp, depending on their composition.

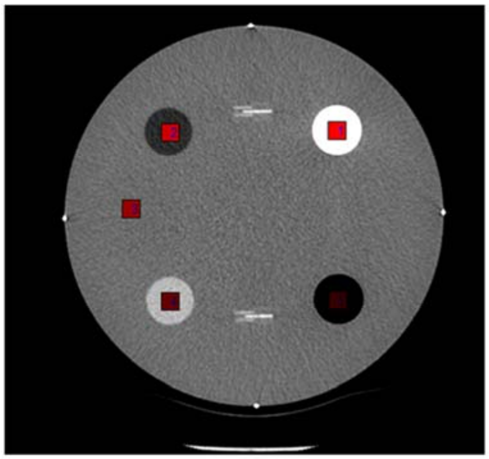

Figure 26. ACR phantom CT value accuracy test module

ACR Material	Target Tissue	Criteria (HU)
Bone equivalent plastic	Bone	850~970
Polyethylene	Fat	-107~87
Water	Water	-7~7
Acrylic	Soft Tissue	+110~135

Table 4: CT value calibration criteria of American College of Radiology (ACR).

Material (Expected CT value)	80kVp (600mA)	140kVp (345mA)	Virtual 120kVp
Bone (950 HU)	1214.9±21.8	837.5±13.0	924.3±11.4
Polyethylene (-95HU)	-118.5±12.9	-80.9±8.3	-89.5±6.8
Water (0HU)	5.0±14.2	5.5±9.8	5.4±8.4
Acrylic (120HU)	111.9±17.8	135.1±10.1	129.7±9.8

Table 5: DECT measurements of CT value accuracy test module. Note that the CT value of acrylic increases at 140kVp, which cannot represent the energy-dependency of soft tissue X-ray attenuation, and notice that the virtual 120kVp has the best accuracy with less noise.

The validity of the proposed model of Eq. (34) was the primary concern in this work. I have not found any significant exception at least in human body tissue. Raptopoulous et al. [33] reported that fatty liver increase CT values up to 15HU at 140kVp, which is within the tolerance of the proposed algorithm. It appears that carbon-rich compounds such as Lucite and acrylic are one of the exceptions. They are heavier than water but increase their CT values at 140kVp. It is due to high contents of hydrogen [58] . Since the materials are not related to body tissues, it was not considered in this technique, but the property of carbon polymers may be utilized for other industrial applications of DECT.

4.6 Image-based and Projection-based Material Decomposition

There are two approaches to material decomposition in DECT. Siemens DSCT uses image-based three-material decomposition, and GE Discovery 750HD uses the projection-based two-material decomposition. Some recent works insist that the projection-based material decomposition is superior to image-based decomposition [34, 68]. In their works, the results of the projection-based method are after the spectral-error correction using the spectral information, but those of the image-base method had beam-hardening correction individually for each X-ray level. The each image of 80kVp and 140kVp was calibrated for the density estimation, not for the spectral information. By its nature, the projection-based method is calibrated using two mixtures of water and iodine.

It is the conventional CT imaging that is inferior to DECT with the aspect of material differentiation. In any DECT application, the result of image-based method should be similar to those of the projection method for material differentiation, as long as the same measurement data and the same reconstruction method were used, because the system equations of Eqs. (26) are the common for both methods. Without any additional assumption or information, only the calibration or noise treatment makes the difference.

The projection-based method has an advantage that the noise can be balanced between low and high energy projection data *before* the reconstruction, and so projection-based image may be better. However, such noise reduction can be done even in an image-based method. This work shows that two reconstructed images can be improved further by correcting the spectral errors and can produce high quality density maps. Material differentiation is improved with the improved high quality density map. With the density maps improved, pseudo-monochromatic images can be generated for the optimal contrast as done in the reference [69].

4.7 Low-kVp-High-Current CT imaging

It is interesting to note that the similarity of the proposed method to sigmoid blending technique [52], in which CT values of low attenuation are extracted from the 140kVp image while CT values of high attenuation are obtained from the 80kVp image and so improve contrast and conspicuity especially for hypervasular tumor. However, their approach is to find the optimal contrast imaging, which is not different from the conventional imaging. This technique is to improve the quality of the spectral information. It is the spectral information that DECT targets to acquire. With the spectral information improved, various application of DECT can be performed like virtual non-contrast imaging, direct differentiation of liver metastases and cysts [34, 69].

Recently, radiologists realized the potential of low-kVp-high-current CT imaging. Low energy CT imaging improves conspicuity especially for hyper-vascular tumors by enhancing contrast between contrast-enhanced tumors and unenhanced surrounding tissues [70, 71]. However, the current x-ray tube technology does not provide enough power to resolve noise problem of the low energy CT imaging. With the advance of x-ray tube technology, the single low energy imaging with high x-ray tube current might be preferred to DECT by radiologist. In a practical point of view, it is the problem of DECT that it provides too much information such as low and high energy images, virtual non-contrast image, and density maps. So, if a single image of low energy CT can provide enough information for malignant tumor detection, it will be preferred by radiologists. Clinicians do active researches to establish new DECT criteria for each target disease. Once DECT imaging criteria are established, all the confusion will be removed. It is no doubt that DECT will become a new standard for detection of abnormality in the human body.

CHAPTER 5

CONCLUSION

In this work, a new model and an image enhancement technique for DECT has been proposed, based on the fact that the attenuation of high density materials decreases relatively faster as X-ray energy increases. Any CT-value pair of low and high energy images which deviates far from the expected trend is considered as noise or error and was called the spectral error of DECT. So, selective processing on spectral errors, the noisy or error pixels, was applied. The proposed technique consists of water-offset correction, spectral error correction, and adaptive noise suppression. It is the main idea of the propose technique to make the spectral errors distributed like random noise over the expected attenuation, mixed and balanced with their neighboring pixels.

The propose technique reduced noise, improved contrast without degrading edge detail because it selectively corrected the spectral errors of DECT images, and it provided better material differentiation in real patient images as well as phantom studies. The improved density maps can be used for the material differentiation and the generation of pseudo-monochromatic images for optimal contrast for each target disease. In addition, the water density map can be used for virtual non-contrast imaging so that it helps to reduce radiation dose by avoiding pre-contrast imaging in the typical contrast-enhanced CT imaging protocols. However, this work is limited to the old DECT system. This work should be validated further for the recent advanced DECT systems which minimized the misregistration problem by the fast acquisition.

CT imaging has been established over 30 years. CT Imaging criteria for various diseases have been established based on the standard 120kVp imaging. However, DECT has just become available for routine clinical imaging. A new standard for DECT calibration and criteria should be established as soon as possible, and then the results of different DECT systems can be compared to each other, and imaging criteria for target diseases can be established. Until such DECT criteria are established, virtual 120kVp image should be used for quantifiable comparison to the standard 120kVp CT criteria.

Radiologists do active research to establish the DECT criteria of various diseases and tissue types, and they already predicted carefully that DECT can be an alternative to PET-CT and SPECT. It is no doubt that DECT will be one of standard CT imaging procedure for routine diagnosis in near future.

REFERENCES

[1] E. C. Beckmann, "CT scanning the early days," *Br J Radiol,* vol. 79, pp. 5-8, Jan 2006.

[2] M. Karcaaltincaba and A. Aktas, "Dual-energy CT revisited with multidetector CT: review of principles and clinical applications," *Diagn Interv Radiol,* Nov 14 2010.

[3] Hounsfie.Gn, "Computerized Transverse Axial Scanning (Tomography) .1. Description of System," *British Journal of Radiology,* vol. 46, pp. 1016-1022, 1973.

[4] J. P. Stonestrom*, et al.*, "A framework for spectral artifact corrections in x-ray CT," *IEEE Trans Biomed Eng,* vol. 28, pp. 128-41, Feb 1981.

[5] W. Marshall*, et al.*, "An implementation of dual energy CT scanning," *J Comput Assist Tomogr,* vol. 8, pp. 745-9, Aug 1984.

[6] A. Macovski*, et al.*, "Energy dependent reconstruction in X-ray computerized tomography," *Comput Biol Med,* vol. 6, pp. 325-36, Oct 1976.

[7] R. E. Alvarez and A. Macovski, "Energy-selective reconstructions in X-ray computerized tomography," *Phys Med Biol,* vol. 21, pp. 733-44, Sep 1976.

[8] C. E. Cann*, et al.*, "Quantification of calcium in solitary pulmonary nodules using single- and dual-energy CT," *Radiology,* vol. 145, pp. 493-6, Nov 1982.

[9] H. I. Goldberg*, et al.*, "Noninvasive quantitation of liver iron in dogs with hemochromatosis using dual-energy CT scanning," *Invest Radiol,* vol. 17, pp. 375-80, Jul-Aug 1982.

[10] A. M. Laval-Jeantet*, et al.*, "A postprocessing dual energy technique for vertebral CT densitometry," *J Comput Assist Tomogr,* vol. 8, pp. 1164-7, Dec 1984.

[11] L. B. Russell*, et al.*, "Dual energy CT scanning for analysis of brain damage due to X-irradiation," *Ann Biomed Eng,* vol. 12, pp. 15-28, 1984.

[12] J. R. Vetter*, et al.*, "Evaluation of a prototype dual-energy computed tomographic apparatus. II. Determination of vertebral bone mineral content," *Med Phys,* vol. 13, pp. 340-3, May-Jun 1986.

[13] W. Kalender*, et al.*, "[Material selective imaging and density measurement with the dual energy method. III. Determination of bone mineral of the spine with CT]," *Digitale Bilddiagn,* vol. 7, pp. 170-6, Dec 1987.

[14] A. E. Burgess*, et al.*, "Vertebral trabecular bone: comparison of single and dual-energy CT measurements with chemical analysis," *J Comput Assist Tomogr,* vol. 11, pp. 506-15, May-Jun 1987.

[15] W. Bautz and W. A. Kalender, "[Material selective imaging and determination of density using the dual energy method. II. Clinical use of dual energy radiography]," *Digitale Bilddiagn,* vol. 7, pp. 95-103, Sep 1987.

[16] E. L. Nickoloff*, et al.*, "Bone mineral assessment: new dual-energy CT approach," *Radiology,* vol. 168, pp. 223-8, Jul 1988.

[17] D. M. Leighton*, et al.*, "Dual energy CT estimation of liver iron content in thalassaemic children," *Australas Radiol,* vol. 32, pp. 214-9, May 1988.

[18] T. R. Johnson*, et al.*, "Dual-source CT cardiac imaging: initial experience," *Eur Radiol,* vol. 16, pp. 1409-15, Jul 2006.

[19] M. Heuschmid*, et al.*, "Usefulness of noninvasive cardiac imaging using dual-source computed tomography in an unselected population with high prevalence of coronary artery disease," *Am J Cardiol,* vol. 100, pp. 587-92, Aug 15 2007.

[20] H. Seifarth*, et al.*, "Optimal systolic and diastolic reconstruction windows for coronary CT angiography using dual-source CT," *AJR Am J Roentgenol,* vol. 189, pp. 1317-23, Dec 2007.

[21] T. G. Flohr*, et al.*, "First performance evaluation of a dual-source CT (DSCT) system," *Eur Radiol,* vol. 16, pp. 256-68, Feb 2006.

[22] S. Achenbach*, et al.*, "Contrast-enhanced coronary artery visualization by dual-source computed tomography--initial experience," *Eur J Radiol,* vol. 57, pp. 331-5, Mar 2006.

[23] H. Scheffel*, et al.*, "Accuracy of dual-source CT coronary angiography: First experience in a high pre-test probability population without heart rate control," *Eur Radiol,* vol. 16, pp. 2739-47, Dec 2006.

[24] G. Bastarrika*, et al.*, "[Dual-source CT coronary angiography]," *Rev Med Univ Navarra,* vol. 51, pp. 4-8, Jul-Sep 2007.

[25] H. Brodoefel*, et al.*, "Dual-source CT with improved temporal resolution in assessment of left ventricular function: a pilot study," *AJR Am J Roentgenol,* vol. 189, pp. 1064-70, Nov 2007.

[26] D. Matt*, et al.*, "Dual-source CT coronary angiography: image quality, mean heart rate, and heart rate variability," *AJR Am J Roentgenol,* vol. 189, pp. 567-73, Sep 2007.

[27] S. Leschka*, et al.*, "Image quality and reconstruction intervals of dual-source CT coronary angiography: recommendations for ECG-pulsing windowing," *Invest Radiol,* vol. 42, pp. 543-9, Aug 2007.

[28] T. R. Johnson*, et al.*, "Evaluation of left atrial myxoma by dual-source CT," *Cardiovasc Intervent Radiol,* vol. 30, pp. 1085-6, Sep-Oct 2007.

[29] A. N. Primak*, et al.*, "Noninvasive differentiation of uric acid versus non-uric acid kidney stones using dual-energy CT," *Acad Radiol,* vol. 14, pp. 1441-7, Dec 2007.

[30] T. R. Johnson*, et al.*, "Material differentiation by dual energy CT: initial experience," *Eur Radiol,* vol. 17, pp. 1510-7, Jun 2007.

[31] D. T. Boll, *et al.*, "Renal stone assessment with dual-energy multidetector CT and advanced postprocessing techniques: improved characterization of renal stone composition--pilot study," *Radiology,* vol. 250, pp. 813-20, Mar 2009.

[32] M. H. Mendler, *et al.*, "Dual-energy CT in the diagnosis and quantification of fatty liver: limited clinical value in comparison to ultrasound scan and single-energy CT, with special reference to iron overload," *J Hepatol,* vol. 28, pp. 785-94, May 1998.

[33] V. Raptopoulos, *et al.*, "Value of dual-energy CT in differentiating focal fatty infiltration of the liver from low-density masses," *AJR Am J Roentgenol,* vol. 157, pp. 721-5, Oct 1991.

[34] E. J. Tkaczky, *et al.*, "Quantization of liver tissue in fast-switched dual kVp computed tomography using linear discriminant analysis," in *Medical Imaging 2009: Physics of Medical Imaging*, Orlando, Florida, USA, 2009.

[35] F. Li, *et al.*, "Improved detection of small lung cancers with dual-energy subtraction chest radiography," *AJR Am J Roentgenol,* vol. 190, pp. 886-91, Apr 2008.

[36] C. Fink, *et al.*, "Dual-Energy CT Angiography of the Lung in Patients with Suspected Pulmonary Embolism: Initial Results," *Rofo,* Sep 10 2008.

[37] S. F. Thieme, *et al.*, "Dual energy CT for the assessment of lung perfusion-Correlation to scintigraphy," *Eur J Radiol,* vol. 68, pp. 369-74, Dec 2008.

[38] E. J. Chae, *et al.*, "Xenon ventilation CT with a dual-energy technique of dual-source CT: initial experience," *Radiology,* vol. 248, pp. 615-24, Aug 2008.

[39] H. W. Goo, *et al.*, "Xenon ventilation CT using a dual-source dual-energy technique: dynamic ventilation abnormality in a child with bronchial atresia," *Pediatr Radiol,* vol. 38, pp. 1113-6, Oct 2008.

[40] B. Ruzsics, *et al.*, "Dual-energy CT of the heart for diagnosing coronary artery stenosis and myocardial ischemia-initial experience," *Eur Radiol,* vol. 18, pp. 2414-24, Nov 2008.

[41] C. Sun, *et al.*, "An initial qualitative study of dual-energy CT in the knee ligaments," *Surg Radiol Anat,* vol. 30, pp. 443-7, Jul 2008.

[42] B. Ruzsics, *et al.*, "Images in cardiovascular medicine. Myocardial ischemia diagnosed by dual-energy computed tomography: correlation with single-photon emission computed tomography," *Circulation,* vol. 117, pp. 1244-5, Mar 4 2008.

[43] A. Persson, *et al.*, "Advances of dual source, dual-energy imaging in postmortem CT," *Eur J Radiol,* vol. 68, pp. 446-55, Dec 2008.

[44] N. Takahashi, *et al.*, "Detectability of urinary stones on virtual nonenhanced images generated at pyelographic-phase dual-energy CT," *Radiology,* vol. 256, pp. 184-90, Jul 2010.

[45] N. Takahashi*, et al.*, "Dual-energy CT iodine-subtraction virtual unenhanced technique to detect urinary stones in an iodine-filled collecting system: a phantom study," *AJR Am J Roentgenol,* vol. 190, pp. 1169-73, May 2008.

[46] A. Graser*, et al.*, "Dual energy CT: preliminary observations and potential clinical applications in the abdomen," *Eur Radiol,* Aug 2 2008.

[47] A. Graser*, et al.*, "Dual-energy CT in patients suspected of having renal masses: can virtual nonenhanced images replace true nonenhanced images?," *Radiology,* vol. 252, pp. 433-40, Aug 2009.

[48] D. Xu*, et al.*, "Dual Energy CT via Fast kVp Switching: Spectrum estimation," in *Medical Imaging 2009: Physics of Medical Imaging*, Orlando, Florida, USA, 2009.

[49] X. Wu*, et al.*, "Monochromatic CT image representation via Fast switching dual kVP," in *Medical Imaging 2009: Physics of Medical Imaging*, Orlando, Florida, USA, 2009.

[50] W. Kalender, *Computed Tomography:Fundamentals, System Technology, Image Quality, Applications*. Erlangen: Publicis Corporate publishing, 2005.

[51] C. A. Coursey*, et al.*, "Dual-energy multidetector CT: how does it work, what can it tell us, and when can we use it in abdominopelvic imaging?," *Radiographics,* vol. 30, pp. 1037-55, Jul-Aug 2010.

[52] D. R. Holmes, 3rd*, et al.*, "Evaluation of non-linear blending in dual-energy computed tomography," *Eur J Radiol,* vol. 68, pp. 409-13, Dec 2008.

[53] R. C. Gilkeson*, et al.*, "Digital radiography with dual-energy subtraction: improved evaluation of cardiac calcification," *AJR Am J Roentgenol,* vol. 183, pp. 1233-8, Nov 2004.

[54] R. C. Gilkeson and P. B. Sachs, "Dual energy subtraction digital radiography: technical considerations, clinical applications, and imaging pitfalls," *J Thorac Imaging,* vol. 21, pp. 303-13, Nov 2006.

[55] J. D. Balkman*, et al.*, "Dual energy subtraction digital radiography improves performance of a next generation computer-aided detection program," *J Thorac Imaging,* vol. 25, pp. 41-7, Feb 2010.

[56] L. G. Dasher*, et al.*, "Dual X-ray absorptiometry in today's clinical practice," *Radiol Clin North Am,* vol. 48, pp. 541-60, May 2010.

[57] L. A. Lehmann*, et al.*, "Generalized image combinations in dual KVP digital radiography," *Med Phys,* vol. 8, pp. 659-67, Sep-Oct 1981.

[58] D. J. Hawkes*, et al.*, "Tissue analysis by dual-energy computed tomography," *Br J Radiol,* vol. 59, pp. 537-42, Jun 1986.

[59] T. C. Gerber*, et al.*, *Computed Tomography of the Cardiovascular system*: Informa Healthcare, 2007

[60] T. R. C. Johnson, "Dual-Energy CT–Technical Background," in *Multislice CT*, M. F. Reiser*, et al.*, Eds., ed: Springer Berlin Heidelberg, 2009, pp. 65-73.

[61] R. J. Warp and J. T. Dobbins, 3rd, "Quantitative evaluation of noise reduction strategies in dual-energy imaging," *Med Phys,* vol. 30, pp. 190-8, Feb 2003.

[62] W. A. Kalender*, et al.*, "An algorithm for noise suppression in dual energy CT material density images," *IEEE Trans Med Imaging,* vol. 7, pp. 218-24, 1988.

[63] C. N. De Cecco*, et al.*, "Dual energy CT (DECT) of the liver: conventional versus virtual unenhanced images," *Eur Radiol,* Jul 11 2010.

[64] K.-K. Park*, et al.*, "Noisy Pixel Detection Scheme for Dual Energy X-ray CT," in *RNSA*, Chicago, IL, USA, 2010.

[65] C. H. McCollough*, et al.*, "The phantom portion of the American College of Radiology (ACR) computed tomography (CT) accreditation program: practical tips, artifact examples, and pitfalls to avoid," *Med Phys,* vol. 31, pp. 2423-42, Sep 2004.

[66] R. T. Gupta*, et al.*, "Dual-energy CT for characterization of adrenal nodules: initial experience," *AJR Am J Roentgenol,* vol. 194, pp. 1479-83, Jun 2010.

[67] R. C. Gonzalez and R. E. Woods, *Digital image processing*. Reading, Mass.: Addison-Wesley, 1992.

[68] D. J. Walter*, et al.*, "Accuracy and precision of dual energy CT imaging for the quantification of tissue fat content," in *Medical Imaging 2006: Physics of Medical Imaging*, San Diego, CA, USA, 2006, pp. 61421G-12.

[69] A. Santamarıa-Panga*, et al.*, "Automated Liver Lesion Characterization using fast kVp switching Dual Energy Computed Tomography Imaging," in *SPIE Medical Imaging 2010*, Orlando,Florida, USA, 2010, pp. 76240V-1.

[70] K. S. Kim*, et al.*, "Image fusion in dual energy computed tomography for detection of hypervascular liver hepatocellular carcinoma: phantom and preliminary studies," *Invest Radiol,* vol. 45, pp. 149-57, Mar 2010.

[71] B. M. Yeh*, et al.*, "Dual-energy and low-kVp CT in the abdomen," *AJR Am J Roentgenol,* vol. 193, pp. 47-54, Jul 2009.